

1 Revision to Geophysical Journal International on August 2013.

2 **Self-induced seismicity due to fluid circulation along faults.**

3

4 Hideo Aochi¹, Blanche Poisson^{1†}, Renaud Toussaint^{2,3}, Xavier Rachez⁴, and Jean Schmittbul²

5 ¹BRGM, Risks and Prevention Division, Orléans, France

6 ²Institut de Physique du Globe de Strasbourg, CNRS UMR7516, University of Strasbourg,
7 Strasbourg, France

8 ³Center for Advanced Study at the Norwegian Academy of Science and Letters, Oslo,
9 Norway.

10 ⁴BRGM, Geothermal Department, Orléans, France

11

12 **Abstract**

13 In this article, we develop a system of equations describing fluid migration, fault
14 rheology, fault thickness evolution and shear rupture during a seismic cycle, triggered either
15 by tectonic loading or by fluid injection. Assuming that the phenomena predominantly take
16 place on a single fault described as a finite permeable zone of variable width, we are able to
17 project the equations within the volumetric fault core onto the 2D fault interface. From the
18 basis of this “fault lubrication approximation”, we simulate the evolution of seismicity when
19 fluid is injected at one point along the fault to model induced seismicity during an injection
20 test in a borehole that intercepts the fault. We perform several parametric studies to
21 understand the basic behaviour of the system. Fluid transmissivity and fault rheology are key
22 elements. The simulated seismicity generally tends to rapidly evolve after triggering,
23 independently of the injection history and end when the stationary path of fluid flow is
24 established at the outer boundary of the model. This self-induced seismicity takes place in the
25 case where shear rupturing on a planar fault becomes dominant over the fluid migration
26 process. On the contrary, if healing processes take place, so that the fluid mass is trapped
27 along the fault, rupturing occurs continuously during the injection period. Seismicity and fluid
28 migration are strongly influenced by the injection rate and the heterogeneity.

29

30

† Deceased 8th December 2011

1 **1. Introduction**

2 Some seismicity is believed to be driven by fluid circulation, because high-pressure fluid in
3 the fault zone can reduce frictional strength. In principal, the following two categories can be
4 identified. The first of these is naturally-occurring induced seismicity, including volcanic
5 seismicity, some aftershocks of large earthquakes, or seismicity in subduction contexts where
6 large quantities of fluid can be expected to be present. In such examples, although the
7 existence of the fluid can be imaged from seismic tomography, it is very difficult to quantify
8 fluid migration and the resultant seismicity. The second category is identified as
9 anthropogenically-induced seismicity, forced by industrial or other forms of manmade
10 injection or extraction of fluid such as the extraction of natural gas, CO₂ storage and the
11 development of deep geothermal systems.
12

13 Many cases of naturally-occurring induced seismicity have been reported over recent
14 decades. One notable example was the Matsushiro earthquake swarm that lasted two years
15 starting in 1965 and featured more than 60 000 felt earthquakes, the largest of which had a
16 magnitude of 5.4. Although various models based on dilatancy and magma-intrusion had been
17 proposed, the events can more probably be ascribed to a massive migration of fluids including
18 outflow to the ground (e.g., Ohtake, 1976; Matsu'ura and Karakama, 2005; Cappa et al.,
19 2009). Some seismic activities triggered in the wake of large earthquakes suggest the
20 important role of fluids, as demonstrated as far away as 1250 km from the epicentral zone in
21 the wake of the 1992 Landers, California, earthquake (Hill *et al.*, 1993). Such triggered
22 earthquake swarms have been observed for other earthquakes too, such as the Yalova cluster
23 that ensued after the 1999 Izmit earthquake (Karabulut *et al.*, 2011) or regional seismicity
24 following the 1997-1998 Umbria-Marche, Italy, sequence (Lombardi *et al.*, 2010).
25 Earthquake migrations have also been observed as a result of the release of CO₂-rich water
26 (Miller *et al.*, 2004). Some crustal earthquakes may have been triggered due to high pore
27 pressure, as inferred for the 2009 L'Aquila, Italy, earthquake (Terakawa *et al.*, 2010).
28 Furthermore, the importance of the existence of fluids has been emphasized for plate
29 boundaries, in particular for subduction associated with microseismicity or aseismic slip.
30 Obara (2002) reported that the discovered deep, non-volcanic tremors along the subducting
31 Philippine Sea plate may be related to the fluid generated by dehydration processes from the
32 slab. In many cases, the existence of fluid is inferred from seismic tomography as an anomaly
33 of V_p/V_s , the ratio of P-wave and S-wave velocities (O'Connell and Budiansky, 1974;

1 Thurber *et al.*, 1997 and others). Seismicity clusters attributed to fluid migration have also
2 been observed in stable tectonic contexts, such as Remiremont, France (Audin *et al.*, 2002).

3
4 On the other hand, it is recognized that seismicity can be induced directly in
5 conjunction with fluid injection (Shapiro *et al.*, 1999, Shapiro and Dinske, 2009), in particular,
6 in deep geothermal projects (Person, 1981; Cornet and Jianmin, 1995; Calò *et al.*, 2011) or
7 CO₂ injection projects (Cappa and Rutqvist, 2011a, 2012; Zoback *et al.*, 2012; Mazzoldi *et al.*,
8 2012). The stimulation phases of the deep geothermal projects, in particular, require
9 seismogenic reactivation of pre-existing fractures or micro-fracturing to allow fluid
10 circulation in the targeted reservoir. Assessing this type of seismicity is, therefore, becoming
11 an important issue. For example, at Soultz-sous-Forêts (Alsace, France), an Enhanced
12 Geothermal System (EGS), has been monitored since an initial borehole was drilled to a depth
13 of 2000 m in 1987 (Kappeimeyer *et al.*, 1991; Beauce *et al.*, 1991; Fabriol *et al.*, 1994; Evans
14 *et al.*, 2005; Neuville *et al.*, 2009, Gentier *et al.*, 2011a, b; Evans *et al.*, 2012). Subsequently,
15 deeper wells were drilled to depths of about 5000 m, and several stimulations were conducted
16 at regular intervals after 2000 (Dorbath *et al.*, 2009). An injection experiment typically lasts a
17 few days (about 100-250 hours), with a maximum injected fluid volume speed of 50 L/s and
18 wellhead pressure of 17 MPa. The total volume of injected fluid amounts to about 20 000-30
19 000 m³. More than 100 000 seismic events were detected in the course of the three stimulation
20 experiments, with rates up to 8000 events per day (Baisch *et al.*, 2010). Typically, the
21 seismicity is localized as a cloud surrounding the injection point, which spatially expands
22 with time (Shapiro *et al.*, 1999). Sometimes a quiet zone appears around the injection point
23 once it has been sufficiently stimulated, while the fluid and seismicity migrate outside. This is
24 known as the Kaiser (1950) effect. Although the seismicity briefly expands in a complex 3D
25 medium, the relocated earthquake locations seem to align along one or more planes, construed
26 to be pre-existing faults at the site (Dorbath *et al.*, 2009; Baisch *et al.*, 2010).

27
28 Naturally-triggered or anthropogenically-induced seismicity models have been
29 developed by various researchers in seismology, rock mechanics and other areas of
30 specialization. For injection experiments, volumetric models (sometimes containing networks
31 of linear or plane fractures) have been considered (Bruehl, 2002, 2007; Gentier *et al.*, 2011a,
32 2011b). However, if the seismicity occurs predominantly along some pre-existing fault(s), a
33 linear fault (in 2D) or a plane fault (in 3D) are often studied (e.g., Blanpied *et al.*, 1992;
34 Segall and Rice, 1995; Baisch *et al.*, 2010; Cappa and Rutqvist, 2011b, 2012). Fault rheology

1 is a key element allowing fluid transport. Early models of fluid-driven seismicity triggering
2 simply considered the pressure balance in broken portions to be instantaneous, corresponding
3 to an assumption of very high porosity in these sections (Miller *et al.* 1996). Since natural
4 materials mostly give rise to low Reynolds numbers, due to their low porosity, more precise
5 models incorporate a finite viscosity and pore-fluid transport through permeable parts
6 (governed by Darcy's law, e.g., Walder and Nur, 1984). When finite compressibility of the
7 fluid plays a role, it is reported that this leads to associated pore pressure diffusion (Shapiro *et*
8 *al.*, 1999, Goren *et al.*, 2010, 2011). This compressibility is shown to be involved in most
9 systems of shear faults, and must be taken into account to understand the evolution of pore
10 pressure around the fault (Goren *et al.* 2010).

11

12 Experimentally, fracturing and finger propagation during fluid injection in analogue
13 faults have been observed at the laboratory scale, in transparent impermeable cells filled with
14 granular materials comparable to fault gouge (Johnsen *et al.*, 2006, 2007, Cheng *et al.* 2008,
15 Huang *et al.* 2012a, 2012b). Similar pattern formations were observed after injection of a
16 slightly compressible and viscous fluid (oil), and of a compressible and slightly viscous
17 substance (air) (Johnsen *et al.*, 2008) – as was the case for the formation of decompaction
18 fronts in such systems (Vinningland *et al.*, 2012). The fracturing and fingering triggered by
19 fluid injection was shown experimentally to be accompanied by microseismicity (Schelstraete,
20 2009).

21

22 To address this type of fluid-driven fracturing, modelling the momentum exchange
23 between the flowing fluid and the elastic solid is essential. When the two are considered as
24 distinct, continuous bodies, mixture theories have been developed that are widely used to
25 model wet landslides (Iverson, 1997). In the context of high fluid flow in highly deformable
26 solids, similar momentum exchanges have been considered between the fluid and discrete
27 element models (Flekkøy *et al.*, 2002, Johnsen *et al.*, 2006). These models have been shown
28 to closely reproduce experimental results, for the deformation of both granular materials
29 saturated with compressible fluids (Vinningland, 2007a, 2007b, 2010) and incompressible
30 ones (Niebling, 2010a, 2010b, 2012a, 2012b). In the present study, we will explicitly take
31 into account the momentum exchange (drag) between the fluid and the deformable solid,
32 considering the finite compressibility and the viscosity of the fluid. An important difference,
33 enabling us to address large systems, is that the solid will be treated here as a continuum with
34 a fault gouge rheology.

1
2
3
4
5
6
7
8
9
10
11
12
13
14
15
16
17

In this study, we build a conceptual simulation model to take into account elastic and plastic porosity changes (e.g., Segall and Rice, 1995) and fault width evolution (e.g., Yamashita, 1999), assuming that the fluid flow and seismicity expand predominantly along a fault plane in a 3D medium. In particular, we address the issue of how induced seismicity, once initiated on a fault, can be brought under control. As we aim to model micro-seismicity, we treat the coseismic rupture process as simply as possible by solving the static equilibrium equations of the elastic medium. In this respect, the approach for the pore pressure and solid stress computations is similar to models developed for fluid injection by Rozhko (2010). Thus, we are not introducing any coseismic thermal effects (Andrews, 2002), which are often discussed for “large” natural earthquakes with large fault slip. The lubrication effect due to pressurized fluid during unstable stages of the dynamics can also be taken into account dynamically (Rice, 2006; Segall and Rice, 2006, Brantut et al, 2011), coupling the fluid dynamics with a discrete elements model to represent the solid (Goren *et al.*, 2011, Ghani *et al.*, 2013).

18 **2. The model**

19 **2.1 Conceptual model of a fault zone**

20 The geological structure and mechanical properties of the earthquake faults have been
21 studied by field observations and drillings for certain active faults (e.g. Chester et al, 1993,
22 Caine et al., 1996; Lockner et al., 2009). The fault core consists of: a rupture trace,
23 surrounded by fault gouge, a damage zone and the surrounding host rock (Figure 1). The
24 hydraulic properties also vary from the fault centre (core) to the host rock,

25 In this study, we will not be considering the poroelastic or the granular nature of the
26 fault core and damage zone. Let us assume that fluid is only allowed within the permeable
27 fault core (e.g., Segall and Rice, 1995; Rice, 2006). We also assume a variable finite width h
28 of the fault core (Yamashita, 1999), as shown in Figure 1. We take the fault core thickness
29 into account when dealing with fluid behaviour, but we consider this thickness to be small
30 enough compared to the fault length for us to be able to calculate the elastic response of the
31 medium due to shear rupture. We then consider that the fluid only circulates in the fault core
32 and that the pore pressure reduces the effective normal stress applied on the fault (as observed

1 at the scale of the fault thickness for impermeable lateral walls, see Goren et al., 2011, among
 2 others). Shear rupture is assumed to be described by the Coulomb criterion (e.g., Terzaghi,
 3 1943). The rupture may change the state of the poroelasticity (e.g., porosity, permeability and
 4 fault width) of the fault core, but we assume that fluid flow and poroelastic response occur at
 5 very different time scales and can accordingly be solved sequentially (see numerical
 6 algorithm of Figure 2).

7 The system of the governing equations for fluid migration in any porous medium is
 8 commonly based on two equations: firstly the linear Darcy's law if the Reynolds number is
 9 sufficiently low (e.g., Chapman, 1981):

$$10 \quad \vec{q} = -\rho \frac{\kappa}{\eta} \nabla P, \quad (1)$$

11 which indicates that fluid mass flux \vec{q} [kg/s/m²] is proportional to the gradient of fluid
 12 pressure with fluid density ρ , fluid viscosity η and permeability κ ; and, secondly, the
 13 continuity of fluid mass:

$$14 \quad \nabla \cdot \vec{q} + \frac{\partial(\rho\phi)}{\partial t} = \rho\dot{\Gamma}, \quad (2)$$

15 where ϕ is porosity and $\dot{\Gamma}$ is the fluid source (volumetric injection rate).

16

17 One of the rheological models most frequently called upon is taken from Walder and
 18 Nur (1994) and Segall and Rice (1995), who write the change in porosity as the sum of elastic
 19 and plastic components:

$$20 \quad \frac{d\phi}{dt} = \dot{\phi}_{elastic} + \dot{\phi}_{plastic} = \frac{\partial\phi_{elastic}}{\partial P} \frac{\partial P}{\partial t} + \dot{\phi}_{plastic} = \phi\beta_{\phi}\dot{P} + \dot{\phi}_{plastic}, \quad (3)$$

21 where β_{ϕ} is the elastic pore compressibility defined by $\beta_{\phi} = (1/\phi)(\partial\phi/\partial P)$. Strictly speaking,
 22 the quantity β_{ϕ} should represent the reversible poroelastic characteristic of the medium in the
 23 case where $\partial\phi_{plastic}/\partial P = 0$. Combining the above equations, we obtain:

$$24 \quad \dot{P}(x, y, z) = \frac{1}{\phi(\beta_f + \beta_{\phi})} \left[\nabla \cdot \left(\frac{\kappa}{\eta} \nabla P \right) - \dot{\phi}_{plastic} + \dot{\Gamma} \right], \quad (4)$$

25 corresponding to Equation (12) in Segall and Rice (1995), Equation (1a) in Wong *et al.*
 26 (1997), Equation (1) in Miller and Nur (2000) and Equation (7) in Goren et al. (2010).

27

2.2. Fault zone boundary condition and governing equation

In this study, we consider that the permeability κ varies along the (x, y) -fault plane as shown in Figure 1. We then integrate Equation (4) over the fault-perpendicular direction (z) for the fault zone as demonstrated in Yamashita (1999). We assume that the fluid does not flow across the interface between the fault core zone and the surrounding, low-permeability rock, at $z = h_+$ and h_- , and that inside the fault core zone, the variables are uniform in the z -direction, as variation along this direction is considered to be smaller than in the (x, y) -directions:

$$\int_{h_-}^{h_+} (\nabla \vec{q} + \dot{m}) dz = \int_{h_-}^{h_+} \rho \dot{\Gamma}(x, y, z) dz \quad (5)$$

which leads to:

$$h \left(\frac{\partial q_x}{\partial x} + \frac{\partial q_y}{\partial y} \right) + [q_z]_{h_-}^{h_+} + h \dot{m} = \rho h \dot{\Gamma}. \quad (6)$$

where the fault core width is expressed by $h = (h_+) - (h_-)$. Note that all the variables are hereafter averaged within the fault core and are a function of (x, y) only. There is no perpendicular flux across the fault boundary due to the impermeability of the surrounding medium, but it is related to the change of the boundary position itself, as follows:

$$q_z = \rho \phi \frac{dh}{dt}. \quad (7)$$

We then obtain:

$$h \left(\frac{\partial q_x}{\partial x} + \frac{\partial q_y}{\partial y} \right) + \rho \phi \frac{dh}{dt} + h \frac{d}{dt} (\rho \phi) = \rho h \dot{\Gamma}. \quad (8)$$

The product of the permeability κ and fault width h is called ‘‘transmissivity’’, which is often used to describe the horizontal water flow in aquifers (e.g. Zimmermann and Bodvarsson, 1996; Zimmermann and Main, 2004). However, for our application, the shear rupturing may greatly change the characteristics of the fault zone in terms of the porosity of the fault core and the fault zone width. If either of these two parameters is unchanged during the process, we could adopt the transmissivity as a model parameter. Now the equation is reduced to a 2D problem (i.e., lubrication approximation). We can, therefore, similarly write, according to Equation (4):

$$\dot{P}(x, y) = \frac{1}{\phi(\beta_f + \beta_\phi)} \left[\nabla \left(\frac{\kappa}{\eta} \nabla P \right) - \phi \frac{\dot{h}}{h} - \dot{\phi}_{plastic} + \dot{\Gamma} \right] \quad (9)$$

This relation is to be compared with Equation (4) with an additional term including h .

1 The mass of the medium should be conserved regardless of the change in porosity:

$$2 \quad \frac{d}{dt}((1-\phi)\rho_\phi h) = 0, \quad (10)$$

3 where ρ_ϕ is the density of medium and then, again using $\beta_\phi = (1/\phi)(\partial\phi/\partial P)$, we obtain the
4 evolution for h :

$$5 \quad \dot{h} = h \left(\frac{\dot{\phi}}{1-\phi} - \beta_\phi \dot{P} \right) \quad (11)$$

6 Compared to the equation in Yamashita (1999), our boundary condition is defined differently
7 so that the conservation of mass is taken into account. Yamashita (1999) treated the fault core
8 width as an independent variable but in our formulation it depends on the other variables,
9 porosity and pressure.

11 2.3. Rupture process and stress redistribution

12 As previously stated, the rupture process is governed by a Coulomb law. An increase
13 in pore pressure plays a role in reducing the fault strength. The fault strength τ_f is expressed
14 as:

$$15 \quad \tau_f = \mu_s \sigma_n^{eff} = \mu_s (\sigma_n - P), \quad (12)$$

16 where μ_s is the static frictional coefficient and σ_n^{eff} is termed effective normal stress, or
17 Terzaghi's normal stress (Terzaghi, 1943). The fact that this effective stress controls shear
18 rupture via a Coulomb law was experimentally established in triaxial laboratory tests, e.g., by
19 Nur and Byerlee (1971). The rupture does not begin if the applied shear stress is lower than
20 the strength. During the rupture, the fault strength reduces gradually with on-going slip (Δu)
21 after a characteristic distance (so-called "slip-weakening distance" and usually called D_c) to
22 the residual stress (dynamic friction) level (Ida, 1972; Palmer and Rice, 1973; Ide and Takeo,
23 1997; Ohnaka, 2003; many others). This weakening process is often written as a simple
24 equation, such as:

$$25 \quad \tau(\Delta u) = \tau_d + (\tau_f - \tau_d) \left(1 - \frac{\Delta u}{D_c} \right) H \left(1 - \frac{\Delta u}{D_c} \right), \quad (13)$$

26 where $H(x)$ is the Heaviside function; $H(x \geq 0) = 1$ otherwise 0. The residual strength
27 (dynamic stress) τ_d is given through a dynamic friction coefficient μ_d ($\mu_d < \mu_s$):

$$28 \quad \tau_d = \mu_d \sigma_n^{eff} = \mu_d (\sigma_n - P). \quad (14)$$

29 The strength drop during an event is accordingly:

$$\Delta\tau = \tau_f - \tau_d = (\mu_s - \mu_d)(\sigma_n - P), \quad (15)$$

if the effective stress does not change during this event. Comparing the fault weakening process during an earthquake, the healing process is not well known. Usually, it is considered that the fault heals over time and shear strength is progressively recovered (Dieterich, 1972). However, the simplest, often used approximations, which are also the most extreme, are immediate healing or no healing.

Equation (13) describes the relation between the on-going slip and strength evolution on the fault. Slip generated on a fault element causes stress increases in the surrounding, so-called “stress redistribution”. For simplicity, the stress redistribution is calculated as a static dislocation problem in an infinite, homogeneous 3D elastic medium, a common procedure in seismology. We regard the shear rupturing as occurring in a very narrow trace within the fault zone. The static response function (Green’s function) can be obtained analytically from the equilibrium equation of elasticity. The discretization on square sub-faults is summarized in Appendix 1 according to Tada *et al.* (2000). Tada *et al.* (2000) integrated the elastodynamic equations by parts (renormalization process) so as to avoid the strong singularity when estimating stress values along the fault, This stress redistribution may let the other fault elements rupture subsequently. We iterate the process one element at a time until all the elements are found to be stable (the imposed stress including the initial one and the perturbation coming from the others is lower than the strength at that time). At last, we can evaluate the seismic moment of one event through the traditional definition used in seismology (e.g. Kanamori and Anderson, 1975):

$$M_0 = \mu \sum_i \Delta u_i \Delta s^2, \quad (16)$$

where Δu_i is the instantaneous fault slip at this time step for ruptured fault element i , and Δs^2 is the element’s surface. One can follow the overall fault evolution with the cumulative fault slip over time.

2.4. Fault porosity and permeability

The link between porosity and permeability plays a crucial role. The permeability value depends strongly on the material and fracture network. Previously, Gentier *et al.* (2011a,

1 b), for example, found κ on an order of 10^{-10} m^2 for a fracture network of the Soultz-sous-
2 Forêt EGS site. Such a large effective permeability indicates that the network is relatively
3 well developed due to fractures and pre-existing fault networks. In laboratory experiments on
4 porous materials, permeability is often about 10^{-18} to 10^{-12} m^2 (strongly dependent on the grain
5 size distribution; e.g. Kozeny, 1927; Carman, 1937; Løvoll et al., 2004; Johnsen et al., 2006;
6 Mavko et al., 2009), and thus the fault in the field must be highly fractured. However, the
7 microscopic rheology that links local porosity and permeability is quite complex, involving
8 plastic deformation processes that are difficult to describe (e.g. Bernarbé et al., 2003). The
9 relations between porosity and permeability are often power laws (e.g. Brace, 1977 and Wong
10 *et al.* 1997), while they may change drastically from one state to another due to the rupturing
11 process (Miller and Nur, 2000). The permeability and the porosity describing the fault state
12 may change according to the fluid migration as well as shear rupturing (Figure 2). This is a
13 key point of the discussion in this study.

14
15

16 **3. Parameter studies**

17 **3.1. Model setting and model parameters**

18 In order to understand the behaviour of our model, this section presents a parametric
19 study. The model parameters we employ are summarized in Table 1. We set an injection rate
20 ($\dot{\Gamma}$) of 31.5 [l/s] during the first 24 hours, for a fault plane consisting of 100×100 elements
21 ($3000 \text{ m} \times 3000 \text{ m}$). Such an injection rate is quite common for EGSs during the stimulation
22 phases (Evans *et al.*, 2012). The injection point, where the injection rate is $\dot{\Gamma}$, is at the fault's
23 centre (everywhere else, the injection rate is nil). The element size is taken to be 30 m, which
24 limits the minimum size of possible earthquake in the simulation scheme. One may question
25 the resolution given by these parameters ; this is discussed in Appendix 2. The slip
26 weakening distance D_c is taken as small enough so that this quantity is practically negligible
27 for the used element size (see also in Appendix 2). At the model boundaries of the given fault
28 plane, we assume drained conditions.

29

3.2. Finiteness of fault core width

We first study some simple situations to understand the role of certain parameters. Let us assume that the permeability is uniform and unchanging, regardless of the fault behaviour and fluid migration (Table 2). In Equation (3), we permit the elastic change of porosity ($\dot{\phi}_{elastic}$), but assume no plastic change ($\dot{\phi}_{plastic} = 0$). The fault width is allowed to vary following Equation (11). We test three different initial fault widths of $h_0 = h|_{t=0} = 1, 3$ and 5 m as the models H1, H3, and H5 shown in Figure 3. We should bear in mind that the fault width h behaves as a scale factor with respect to the permeability κ . In this configuration, fluid behaviour is not linked with fault shear rupture (see also a snapshot at time $t = 80\,000$ s). Firstly, based on the assumed injection, pore pressure continues to increase at the fault's centre. Then it decreases to zero after the end of the injection according to the diffusion term of Equation (9) and a drained condition at the model boundaries. From a physical point of view, pore pressure cannot be allowed to increase above a certain level. The upper limit, therefore, is set at 40 MPa in these simulations in order to guarantee that the effective stress remains positive. Physically, this represents a hydraulic fracture mechanism, where the confining walls of the fault fracture at this value limit the pressure at this saturation level. Numerically, when P exceeds the upper limit, we impose $\dot{P} = 0$. Consequently, the system absorbs the fluid mass change by increasing the fault width h . This type of feedback should operate automatically in real cases. In model H1 ($h_0 = 1$ m) in Figure 3(A), the pore pressure immediately rises to the imposed upper value (i.e., when we do not apply this upper limit, the pore pressure exceeds the confining pressure). A significant increase in fault width (of about 10 %) and porosity (300 %, also imposed as an upper limit) are necessary to absorb the injected fluid mass, while those changes are negligible for the other two cases.

Seismicity is triggered by an increase in pore pressure; that is, the peak shear stress required for rupture decreases versus the injection in model H3 ($h_0 = 3$ m) in Figure 3(B). But soon the shear stress increase soon comes to play a role in subsequent rupturing. In the shown example, the main swarm of seismicity ends with the largest event of $M_w \sim 4.3$ (ruptured dimension is 7.7 km^2 , or 8558 elements). After the largest event, moderate seismicity continues and then decays slowly. The final event occurs half an hour after the injection has stopped in the case of $h_0 = 3$ m. Several earthquakes have a magnitude of $M_w \sim 1.4$, corresponding to the imposed minimum possible dimension of the potentially ruptured fault segment in the model, set to $\Delta s = 30$ m.

1
2
3
4
5
6
7
8
9
10
11

When the fault width is large enough (model H5: $h_0 = 5$ m in Figure 3(C)), we observe that the fluid circulates rapidly without any significant pore pressure increase. Thus, significant seismicity is not induced by the fluid injection. Achieving this condition is the objective of industry-related fluid circulation. However, since we are interested in how the seismicity evolves in our formulated system, we adopt the case of $h_0 = 3$ m as our reference for discussing the effects of various parameters and mechanics. We note here for our later discussion that the permeability κ is required to be an order of 10^{-13} m² for a fault width of $h = 3$ m for the shear rupturing to occur without increasing the pore pressure by too much (Table 2).

12 **3.3. Permeability evolution**

13 The fault property (porosity and permeability) evolves with time following the
14 rupturing. In Equation (3), the first term originating from the elastic change of the porosity
15 ($\dot{\phi}_{elastic}$) is practically negligible, because it is estimated as of an order of 10^{-4} [s⁻¹] for a
16 porosity of 0.1 and a numerically possible change in pressure (\dot{P}) of 10^7 [MPa/s]. As seen in
17 the later simulations, pressure changes are never so rapid in the considered cases. Therefore,
18 the second term ($\dot{\phi}_{plastic}$) may play a practical role, but the definition of $\dot{\phi}_{plastic}$ still remains
19 quite uncertain. Segall and Rice (1995) introduced a relation that is analogous to the state
20 variable evolution of the rate- and state-dependent friction law. Yamashita (1999) describes
21 the plastic porosity as slip (Δu)-dependent:

22
$$\phi_{plastic} = \phi_{ss} + \Delta\phi \exp(-\Delta u / u_c) \tag{17}$$

23 where ϕ_{ss} , $\Delta\phi$ and u_c are constant. Besides, the relation between the permeability and the
24 porosity may be written as (e.g. Brace, 1977):

25
$$\kappa = \kappa_0 (\phi / \phi_0)^n \tag{18}$$

26 where κ_0 , ϕ_0 and n are constant. We tried to use these relations (Appendix 3). However the
27 permeability does not always increase significantly and thus the pore pressure tends to
28 increase easily in Equation (9), namely the insufficient increase in the porosity (the terms
29 $\nabla((\kappa / \eta)\nabla P)$ and $\dot{\phi}_{plastic}$) does not always cancel the injection term ($\dot{\Gamma}$). In other words,

1 alternative evolution of κ is necessary due to the external conditions (rupturing, stress, etc.)
2 rather than the internal relations, such as Equations (17) and (18).

3 Therefore, we adopt the toggle switch (e.g. Miller and Nur, 2000) in which the
4 permeability changes independently from the change in porosity. For simplicity, we introduce
5 two irreversible phases locally according to the state of the fault at each point, i.e., intact or
6 already ruptured:

$$7 \quad \kappa(x, y) = \begin{cases} 10^{-14} m^2 & \text{for } u(x, y) = 0 \\ 10^{-13} m^2 & \text{for } u(x, y) \neq 0 \end{cases} \quad (19)$$

8 where u is the cumulative slip ($u = \sum \Delta u$). Thus, the value is initially small everywhere, and
9 once rupture has occurred, permeability increases up to a constant value of $10^{-13} m^2$. The
10 value of $10^{-14} m^2$ assigned to the material before shear rupture took place might be much
11 smaller as in granular materials; however, the simulation is not influenced, as the given value
12 is quite small so that the fault is practically impermeable at the time scale of our interest. No
13 plastic change in porosity is assumed ($\dot{\phi}_{plastic} = 0$), as the permeability is no longer related to
14 the porosity. The term $\nabla((\kappa/\eta)\nabla P)$ is dominant in Equation (9). We show the simulation
15 results (hereafter referred as model K2) in Figure 4. The other parameters are the same as for
16 model H3 in Figure 3(B). As the pore pressure increases along the boundary of permeability
17 contrast, that is, at the front of the rupture zone, seismicity migrates away from the injection
18 point. Seismicity is far more pronounced than model H3 in Figure 3(B): the rupture front
19 advances gradually, step by step. The pore pressure does not increase beyond the rupture front
20 due to the low permeability, so that it is difficult for rupture to occur there, while in the
21 previous case, the pore pressure increases over a wide area. The assumption of such an abrupt
22 change in permeability due to fracturing leads to seismicity being caused by fluid migration as
23 the injection continues.

24

25

26 **3.4. Heterogeneity in stress field and fault strength**

27 The origin of the heterogeneity observed in earthquake dynamics (e.g. Kanamori and
28 Stewart, 1978; Aki, 1979) is a fundamental question in seismology. Schmittbuhl *et al.*, (2006)
29 study the stress field of the Nojima fault before and after the 1995 Kobe, Japan, earthquake
30 and propose that the fluctuations of the stress field along the fault would be dominated by
31 “quenched” fault properties rather than dynamic stress fluctuations produced during the

1 earthquake. Let us study the effect of heterogeneity in initial shear stress or in fault strength
 2 on the produced seismicity. The meaning of heterogeneity differs for the stress field and the
 3 fault strength, since the former can be released by a rupture while the latter may remain
 4 indefinitely despite repeated ruptures. We first furnish a heterogeneous shear stress, simply
 5 assuming a periodic variation according to a single Fourier mode approach as a first step,
 6 although the actual stress field could be a superposition of different characteristic lengths of
 7 heterogeneity (e.g., Mai and Beroza, 2002):

$$8 \quad \tau_0 = T_0 \times [1 - \delta \cdot f(x, y)] \quad (20)$$

9 where $f(x, y) = \sin(2\pi x / \lambda_x + \alpha_x) \sin(2\pi y / \lambda_y + \alpha_y)$ is a function of position (x, y) , λ_x and λ_y
 10 are the given wavelengths in spatial heterogeneity, and α_x and α_y are random numbers. The
 11 variable δ indicates the amplitude of the heterogeneity, namely a ratio with respect to the
 12 absolute amplitude. In Figure 5, we show the simulation results for (A) model K2_ST10 with
 13 δ of 10 % ($\delta = 0.1$) and (B) model K2_ST20 with $\delta = 0.2$, taking $\lambda_x = 300$ m and $\lambda_y = 500$ m,
 14 respectively. Introducing the heterogeneity leads to more overpressure locally and yields more
 15 earthquakes comparing to model K2 of Figure 4. The snapshots are also shown for model
 16 K2_ST20 with $\delta = 0.2$ (i.e., 20 %) at different times (Figure 5). The expansion of the ruptured
 17 area is heterogeneous and complex in space. In snapshot (1), we note that the area of slip
 18 extends slightly further along the y-axis because of the longer wavelength of the
 19 heterogeneity. For instance, Perfettini *et al.* (2001) numerically study the correlation of the
 20 slip pattern and strength heterogeneity in seismic cycles and find that the slip appearance
 21 reflects the background strength heterogeneity. This is also the case in our simulation. When
 22 the fault has almost entirely ruptured, the fluid circulation becomes quasi-uniform because of
 23 the homogeneous permeability in the ruptured area. At this time, some areas remain
 24 unruptured (snapshot at time (2) in Figure 5).

25 Similarly, we study the effects of spatial heterogeneity for the other parameters. The
 26 fault strength, i.e., the static frictional coefficient, is given a variation based on the reference
 27 frictional coefficient μ_{s0} :

$$28 \quad \mu_s(x, y) = \mu_{s0} \times \{1 + var \cdot (\mu_{s0} - \mu_d) f(x, y)\} \quad (21)$$

29 where the same variation function $f(x, y)$ as in Equation (20) is used. We note that normal
 30 stress itself does not change since we are considering a planar fault, but the effective normal
 31 stress changes due to the pore pressure change (Equation (12)). The dynamic frictional

1 coefficient μ_d is assumed to be uniform everywhere. The relation in Equation (21) represents a
2 continuous change, but we also assume heterogeneity in the discontinuously localised forms:

$$3 \quad \mu_s(x, y) = \begin{cases} \mu_{s0} \times \{1 + var \cdot (\mu_{s0} - \mu_d)\} & \text{if } f(x, y) \geq 0.8 \\ \mu_{s0} & \text{otherwise} \end{cases} \quad (22)$$

4 Fault strength after the first rupture is always heterogeneous according to Equations (21) and
5 (22). We show, in Figure 6, the snapshots for two cases, (A) model K2_TC20 using
6 Equations (21) and (B) model K2_TD20 using Equation (22), with $\delta = 0.5$ (50 %), that is, the
7 maximum value of a given μ_s is 0.975. Slightly more earthquakes are observed in model
8 K2_TD20 (B) than model K2_TC20 (A) from the histograms. Behind the rupture front, in
9 model K2_TD20 (B), the heterogeneity remains visible and the overall fault slip is smaller
10 when comparing the two snapshots at $t = 16\,000$ s. From these simulations, we discover that
11 discontinuous localised heterogeneity affects the details of the rupture growth. The rupture
12 front shape becomes very heterogeneous, and heterogeneous slip distribution persists behind
13 the rupture front. As a result, the total slip is reduced.

14

15 **3.5. The appearance of seismicity**

16 In Figure 7, we analyse the magnitude-frequency relation from some of the simulated
17 seismicity catalogues. In all cases, we obtain the classic power law relation known as
18 Gutenberg-Richter (Gutenberg and Richter, 1954) with a slope of about -1. Large-magnitude
19 events have only a single sample for a given magnitude range of 0.1, and they seem to diverge
20 from the power law. However, the ruptured area for large events reaches the model boundary,
21 so this point should be regarded with caution.

22

23 In general, the number of earthquakes increases at the same time as larger-magnitude
24 earthquakes appear. Pore pressure increases until a large earthquake ($M_w > 4$) occurs,
25 creating a continuous fluid path to the drained model boundary, i.e., a breakthrough. Once this
26 happens, the system becomes stable, and the level of seismicity reduces. This silence is
27 somehow an artificial effect, as the size of the maximum event and the ruptured area is limited
28 by the *a priori* model dimension. However, seismic hazard assessment for induced seismicity
29 in geothermal sites is a major concern (e.g., Majer *et al.*, 2007; Baisch *et al.*, 2009), although
30 phenomena are not completely understandable mechanically (Majer *et al.*, 2012).

31

4. The potential for seismicity control

4.1. The effect of injection and spontaneous seismicity propagation

A challenging question is to find out how the seismicity can be controlled by the injection. We reduced the injection rate by ten compared with the previous cases and its duration to a few hours instead of one day, expecting to observe an evolution in seismicity (or no seismicity) once injection had ceased.

As shown in Figure 8, we simulate two cases under the homogeneous condition (A: model K2_I1) similar to model K2 in Figure 4 and heterogeneous initial shear stress (B: model K2_ST20_I2) like model K2_ST20 with $\delta = 0.2$ (20 %) of Figure 5. The onset of induced seismicity is delayed simply because it takes much more time for sufficient pore pressure to build up at the injection point, while the duration of seismicity does not change visibly as compared to previous cases. The duration of the injection is three and four hours respectively. The difference in injection duration comes simply from the fact that the given heterogeneity (model K2_ST20_I2) needs a greater concentration of pore pressure at the injection point. In both cases, the injection is stopped just after the seismicity began. However, the seismicity continues to propagate and eventually ruptures the entire model fault. We also notice that introducing heterogeneity does not affect this rupture expansion, although it does generate much more seismicity and pore pressure remains relatively high. The rupture progress is locally somehow blocked by the heterogeneity but continues on to the end when the fault system is relaxed.

We conclude that it is very difficult to control seismicity through injection under the given conditions. Once induced, the seismicity propagates rather spontaneously, probably because the heterogeneity considered in this study might still be too small in amplitude and too short in its characteristic correlation length of heterogeneity (Perfettini *et al.*, 2001). The expansion rate of seismicity is insensitive to differences in injection protocol. The shear rupture spontaneously triggers other ruptures to the surrounding area. In this sense, the seismicity is self-induced once started. The mechanism might be similar to the propagation of solitary dislocation propagation (Schmittbuhl *et al.*, 1993), or to Bürgers-like solitons evidenced theoretically for the propagation of overpressure pulses in mud volcanoes (Garcia

1 *et al.* 2000, Revil 2002). The source of this mechanism lies in the nonlinear diffusion process
2 for the fluid pressure, arising due to the pressure dependence of the permeability.

4 4.2. Fault healing and trapped fluid circulation

5 The real permeability of the fault should be more complex than given by Equation (19).
6 We observe that in all the previous simulations, pore pressure finally drops to zero once
7 injection stops. All the injected fluid flowed out from the model boundary as the fault became
8 sufficiently permeable. In reality, the permeability may decrease over time to disturb the fluid
9 circulation and trap it. Let us, therefore, introduce the temporal evolution (sealing) of
10 permeability relative to fault healing, analogous to Aochi and Matsu'ura (2002):

$$11 \quad \frac{d\kappa}{dt} = -\beta(\kappa(t) - \kappa_{\infty}) \quad (23)$$

12 where the parameter $1 / \beta$ provides the characteristic time so that the permeability converges
13 to the final value of κ_{∞} . We do not seek to determine here whether the mechanism of the
14 healing process is mechanical or chemical. For the sake of simplicity, we assume
15 $\kappa_{\infty} = \kappa(t=0)$; however, the fault core may take on a new value, different from the initial
16 permeability, because of the development of a micro-fracture network and the shear rupture.
17 No healing takes place in the limit of $\beta=0$, and $\beta = 1/(432,000 \text{ s}) = 1/(5 \text{ days})$ does not
18 produce any visible effect on the simulation. On the other hand, a large β value indicates a
19 rapid healing of the permeability. For example, in the case of $\beta = 1/(60 \text{ s})$, the healing is
20 exceedingly fast, and pore pressure becomes very high at the injection point. In our current
21 system, the fluid circulation is allowed, not during the coseismic event, but after this rupture.
22 However, the permeability becomes low again soon after the rupture. Thus the fluid
23 circulation is limited. If we allow fluid migration during the event, say $\kappa = \infty$ on the
24 concerned fault segments during rupture (Miller and Nur, 2000), it would be possible to
25 introduce an immediate healing process.

26
27 In Figure 9, we show a typical intermediate case of $\beta = 1/(21\,600 \text{ s}) = 1/(6 \text{ hours})$,
28 model K2_B6, under the same conditions as model K2 in Figure 4. After the first swarm of
29 seismicity terminated by rupture of the entire fault (the first six hours), there is a period of
30 quiescence. This quiet period allows time for the fault to heal, specifically because of the
31 decrease in permeability in the fault zone. As a result, the fluid starts to be trapped, and since

1 fluid is continuously injected, seismic activity resumes once again releasing fluid. After the
2 end of the injection, the fluid is not completely drained due to this sealing effect. Thus, the
3 pore pressure remains at a certain finite value. In a natural context, such distinct swarms may
4 not be identified, as the system can be expected to be more complex and heterogeneous than
5 the simplified model (a single, uniform parameter of sealing). The fact that the system transits
6 from a continuous activity to an intermittent one when β increases is the analogue, in induced
7 seismicity, to the transition observed for fault activities under tectonic loading, when the
8 healing process changes from slow to fast rates – as was observed and explained along the
9 San Andreas Fault (Gratier, 2011, Gratier *et al.*, 2011).

10
11 We now try to emphasize the healing effect on the seismicity and fluid circulation, by
12 reducing the injection time and assuming $\beta = 1/(3\ 600\ \text{s}) = 1/(1\ \text{hour})$. We test homogeneous
13 and heterogeneous initial shear stress ($\delta = 0.2$) with wavelengths of $\lambda_x = \lambda_y = 300\ \text{m}$,
14 respectively (A: model K2_B1, and B: model K2_SH20_B1 in Figure 10). This version of the
15 model reproduces the seismicity without fracturing the whole model fault and the trapped
16 fluid effect without breakthrough. The pore pressure after the end of injection decreases not to
17 zero but to a finite value. Unlike the previous simulations, we also find that heterogeneity
18 plays an important role. In model K2_B1 in Figure 10(A), homogeneous initial shear stress
19 (the same as for model K2 in Figure 4 except for β), seismicity gradually but rapidly ceases
20 after the end of the injection (1 hour). In model K2_SH20_B1 (Figure 10(B)) employing
21 heterogeneous initial shear stress, it takes a much longer time for the seismicity to subside.
22 The seismicity rate (number per hour) significantly increases after the end of the injection,
23 and we observe an earthquake of magnitude 4.39 triggered close to the model boundary. This
24 significant perturbation can be due to the particular distribution of heterogeneity. However,
25 the seismicity ceases after approximately nine hours and fluid is ultimately trapped on the
26 healed fault with a relatively high pore pressure.

27 28 **4.3 Fault interaction**

29 One of the major hypotheses in this study is that the rupture process is restricted to a
30 single fault plane. In this case, the stress redistribution is carried out strictly following the
31 equations in Appendix A, bringing stress disturbance at any distance. However, as previously
32 treated in Baisch *et al.* (2010), let us assume that the stress disturbance only affects the

1 neighbouring elements, namely, $G_{(i-l)(j-m)} = 0$ for $|i-l| > 1$ or $|j-m| > 1$ in Equation (A2).
2 This extreme condition may correspond to a segmentation of the fault off the major plane.

3
4 We show an example of seismicity evolution according to the given injection rate
5 (model SB in Figure 11). This time, rupture is significantly influenced by the injection
6 process despite the fact that the ruptures grows quickly independently of the injection rate. In
7 order to demonstrate how the seismicity is sensitive to the injection protocol, we assume a
8 synthetic injection protocol varying during 2.5 days. We also introduce a relation for the
9 permeability evolution such that it increases by 50 % with every rupture until the upper limit.
10 The seismicity increases during the course of the injection and reducing the injection rate
11 decreases the seismicity. When the injection rate increases once again the seismicity starts to
12 evolve. The seismicity continues during the whole duration of the injection and after its end.

13
14 The effect of stress redistribution is important in governing the induced seismicity.
15 The structure of natural fault systems can be more complex rather than a single fault plane. It
16 is worth of pointing out that stress redistribution on a single planar fault tends to accelerate
17 the rupture growth rapidly, namely “self-induced” seismicity, independent of the injection
18 protocol.

19

20 **5. Discussion**

21 A simple spring-block model does not take into account the elastic response at
22 distance, but only distributes the stress over neighbouring elements, so that the initially
23 imposed heterogeneity also generates a strong heterogeneity in stress and fault slip (e.g., Bak
24 and Tang, 1989). On the other hand, elastic systems which have remote responses (e.g., Rice,
25 1993) behave in such a way as to homogenize both stress and slip. The friction law assumed
26 in this study does not consider any evolution process during a single coseismic event; that is,
27 it lacks a length scale such as characteristic slip distance. Thus, inherently, our discrete
28 system might display spatio-temporal complexity, but globally over a large spatial scale and a
29 long time scale, the simulation finishes when the fault has completely ruptured and/or a
30 stationary injection flow is established from the injection point to the outer boundary of the
31 model. All the simulations display spatial migration, with many events statistically

1 reproducing the scheme of the Gutenberg-Richter magnitude frequency relation. Once
2 seismicity is induced, we see that it is difficult to control because the shear rupture process
3 becomes dominant. This self-induced behaviour is different from any model simulated by a
4 spring-block model of interaction with the immediate neighbourhood (Baisch *et al.*, 2010).

5
6 We summarize the spatio-temporal evolution of the seismicity simulated in this study
7 (Figure 12). The seismicity, once induced by the injection, clearly propagates rather
8 spontaneously, independently of the injected fluid in our simulations. Seismicity migration is
9 often represented in the form:

$$10 \quad r = \sqrt{4\pi Dt} \quad (24)$$

11 where r is the distance of the seismicity front from the injection point, t is the time since the
12 injection onset and D is hydraulic diffusivity (e.g., Shapiro and Dinske, 2009). Shapiro and
13 Dinke (2009) also report that there are some local clouds presenting a very rapid linear trend
14 of seismicity migration that may be related to the fracture opening and reopening.
15 Conceptually, our single-fault core model corresponds to the latter situation.

16
17 In our simulated system, we find that the evolution of fault permeability is essential.
18 We have considered the hypothesis in which the permeability immediately increases after
19 fracturing and gradually decreases with time, given by the simple constitutive relations in
20 Equations (17) and (23). The form of these equations is still to be explored, as many
21 researchers propose different evolution laws and extreme values are possible (e.g., Miller and
22 Nur, 2000); this said, our idea is qualitatively consistent with earlier conceptions (e.g., Miller
23 and Nur, 2000). But permeability may increase even before or during rupture, and aseismic
24 slip is possible (Calò *et al.*, 2011). We have simplified our 3D system to a projected 2D fault
25 model using the hypothesis that fluid migration and fault movement occur dominantly within
26 a fault core. All of the injected fluid mass must circulate within the fault core along the fault
27 plane and no loss is allowed off plane. No extraction from other wells is considered but
28 further studies would be called for. In the field, the seismicity may not always be aligned on a
29 single plane but it may be clustered in a 3D volume. We also find that the pore pressure
30 sometimes becomes extremely high when the given injection rate, permeability, porosity and
31 fault width are not suitable. However, in a real system there should be some mechanical
32 feedbacks between these parameters as well as an off-plane loss mechanism to keep pore
33 pressure reasonable at any given time.

1
2
3
4
5
6
7
8
9
10
11
12
13
14
15
16
17
18
19
20
21
22
23
24
25
26
27
28
29
30
31
32

6. Conclusion

We developed a system of equations describing fluid migration, fault rheology and shear rupture. Assuming that the phenomena predominantly take place on a single fault with a finite permeable zone of variable width, we are able to project the volumetric fault core equations onto the 2D fault plane by introducing a redefined boundary condition of Equation (10). Then we propose a toggle-switch type evolution of fault core permeability, Equation (19), and a healing process, Equation (23). Several parametric studies are performed to understand the basic behaviour of the system established by injecting the fluid at a single point. Fault rheology is a key element. In the absence of fault healing (no decrease in permeability) after rupture, seismicity is generally self-induced, e.g. tends to evolve spontaneously once it is triggered, independently of the injection, and the fluid is completely drained. However, when a sufficiently rapid healing process takes place, the fluid mass is locally trapped along the fault and rupture migration can occur repeatedly. The pore pressure remains high after the end of the injection. The effect of segmentation of stress redistribution in the simulation has been studied and, in such cases, the system is sensitive to the injection protocol.

In this study, we have not precisely calibrated each parameter for specific examples of induced seismicity. The model developed in this study is general for different aspects of seismicity, such as plate boundaries, which may involve large amounts of fluid, as well as for earthquakes induced following injection or extraction of fluid or gas into or out of reservoirs.

Acknowledgments

We deeply regret that Dr Blanche Poisson passed away at the age of only 36 years on 8th December 2011. We would like to acknowledge her important contribution to the early stages of this study. The final version of the article was revised by the other four authors. We thank two anonymous reviewers for their comments, which have significantly improved the manuscript. This work was undertaken in the framework of the French national project ANR SUPNAF (2009 – 2011) and subsequently has been conducted under the European project FP7 GEISER (2010 – 2013) and Labex G-EAU-THERMIE PROFONDE. We also

1 acknowledge the support of the INSU programs DyETI, CESSUR and NEEDS MIPOR, the
2 ANR LANDQUAKE, the ITN FLOWTRANS, and REALISE, a regional Alsatian program.
3 We have also benefited from the support of BRGM funding. Finally, we thank John Douglas
4 for proof reading.
5

6 **References**

- 7 Aki, K. (1979), Characterization of barriers of an earthquake fault, *J. Geophys. Res.*, 84,
8 6140-6148.
- 9 Andrews, D. J. (2002), A fault constitutive relation accounting for thermal pressurization of
10 pore fluid, *J. Geophys. Res.*, 107, 2363, doi:10.1029/2002JB001942.
- 11 Aochi, H. and S. Ide (2009), Complexity in earthquake sequences controlled by multiscale
12 heterogeneity in fault fracture energy, *J. Geophys. Res.*, 114, B03305,
13 doi:10.1029/2008JB006034.
- 14 Aochi, H. and M. Matsu'ura (2002), Slip- and time-dependent fault constitutive law and its
15 significance in earthquake generation cycles, *Pageoph*, 159, 2029-2044.
- 16 Audin, L., J.-P. Avouac, M. Flouzat, and J.-L. Plantet (2002), Fluid-driven seismicity in a
17 stable tectonic context: The Remiremont fault zone, Vosges, France, *Geophys. Res.*
18 *Let.*, 29(6), 1091, doi:10.1029/2001GL012988.
- 19 Baisch, S. Carbon, D., U. Dannwolf, B. Delacou, M. Devaux, F. Dunand, R. Jung, M. Koller,
20 C. Martin, M. Sartori, R. Secanell and R. Vörös (2009), Deep Heat Mining Basel –
21 Seismic Risk Analysis, report of SERIANEX project, <http://wsu.bs.ch/geothermie>.
- 22 Baisch, S., R. Vörös, E. Rothert, H. Stang, R. Jung and R. Schellschmidt (2010), A numerical
23 model for fluid injection induced seismicity at Soultz-sous-Forêts, *Int. J. Rock Mech.*
24 *Min. Sci.*, 47, 405-413.
- 25 Bak, P. and C. Tang, Earthquakes as self-organized critical phenomena (1989), *J. Geophys.*
26 *Res.*, 94, 15635-15637.
- 27 Beauce, A., F. Fabriol, D. LeMasne, C. Cavoit, P. Mechier and X. K. Chen, Seismic studies
28 on the HDR site of Soultz-Forêts (Alsace, France) (1991), *Geotherm. Sci. Tech.*, 3, 239.
- 29 Bernabé, Y., U. Mok and B. Evans (2003), Permeability-porosity relationships in rocks
30 subjected to various evolution processes, *Pure appl. Geophys.*, 160, 937-960.
- 31 Blanpied, M. L., D. A. Lockner and J. D. Byerlee (1992), An earthquake mechanism based on
32 rapid sealing of faults, *Nature*, 358, 574-576.

- 1 Blaupied, M. L., T. E. Tullis and J. D. Weeks (1998), Effects of slip, slip rate, and shear
2 heating on the friction of granite, *J. Geophys. Res.*, 103(B1), 489-511.
- 3 Brace, W. F. (1977), Permeability from resistivity and pore shape, *J. Geophys. Res.*, 82, 3343-
4 3349.
- 5 Brantut, N., J. Sulem, and A. Schubnel (2011), Effect of dehydration reactions on earthquake
6 nucleation: Stable sliding, slow transients, and unstable slip, *J. Geophys. Res.*, 116 ,
7 B05304, doi:10.1029/2010JB007876.
- 8 Bruel, D. (2002), Impact of induced thermal stresses during circulation tests in an engineered
9 fracture geothermal reservoir, *Oil & Gas Sci. Tech. Rev. IFP*, 57, 459-470.
- 10 Bruel, D. (2007), Using the migration of the induced seismicity as a constraint for fracture Hot
11 Dry Rock reservoir modelling, *Int. J. Rock Mech. Min. Sci.*, 44, 1106-1117.
- 12 Carman, P. (1937), Fluid flow through granular beds, *Trans. Inst. Chem. Eng.* 15, 150.
- 13 Calò, M., C. Dorbath, F. H. Cornet and N. Cuenot (2011), Large-scale aseismic motion
14 identified through 4-D P-wave tomography, *Geophys. J. Int.*, 186, 1295-1314.
- 15 Caine, J.S., Evans, J.P., Foster, C.G. (1996). Fault zone architecture and permeability
16 structures. *Geology* 24 (11), 1025–1028.
- 17 Cappa F. and J. Rutqvist (2012). Seismic rupture and ground accelerations induced by CO2
18 injection in the shallow crust. *Geophysical Journal International*, 190, 1784–1789.
- 19 Cappa F. and J. Rutqvist (2011a). Modeling of coupled deformation and permeability
20 evolution during fault reactivation induced by deep underground injection of CO2.
21 *International Journal of Greenhouse Gas Control*, 5, 336–346.
- 22 Cappa F. and Rutqvist J. (2011b). Impact of CO2 geological sequestration on the nucleation
23 of earthquakes. *Geophysical Research Letter*, 38, L17313, doi:10.1029/2011GL048487.
- 24 Cappa F., Rutqvist J., and Yamamoto K (2009). Modeling crustal deformation and rupture
25 processes related to upwelling of deep CO2 rich fluids during the 1965-1967 Matsushiro
26 Earthquake Swarm in Japan. *Journal of Geophysical Research*, 114, B10304.
- 27 Carman, P. C. (1937), Fluid flow through granular beds, *Trans. Inst. Chem. Eng.*, London, 15,
28 150-166.
- 29 Chapman, R. E. (1981), *Geology and water*, Kluwer Boston, Inc., USA.
- 30 Cheng, X., L. Xu, A. Patterson, H. M. Jaeger & S. R. Nagel (2008), Towards the zero-
31 surface-tension limit in granular fingering instability, *Nature Physics* 4, 234 – 237.
- 32 Chester, F. M., J. P. Evans and R. L. Biegel, Internal structure and weakening mechanisms of
33 the San-Andreas fault, *J. Geophys. Res.*, 98, 771-786, 1993.

- 1 Cornet, F. H. and Y. Jianmin (1995), Analysis of induced seismicity for stress field
2 determination and pore pressure mapping, *Pageoph*, 145, 677-700.
- 3 Dieterich, J. (1972), Time-dependent friction in rocks, *J. Geophys. Res.*, 77, 3690-3697.
- 4 Dorbath, L., N. Cuenot, A. Genter, and M. Frogneux (2009), Seismic response of the
5 fractured and faulted granite of Soultz-sous-Forêts (France) to 5 km deep massive water
6 injections, *Geophys. J. Int.*, 177, 653-675.
- 7 Evans, K. F., H. Moriya, H. Niitsuma, R. H. Jones, W. S. Phillips, A. Genter, J. Sausse, R.
8 Jung, and R. Baria (2005), Microseismicity and permeability enhancement of
9 hydrogeologic structures during massive fluid injection into granite at 3 km depth at the
10 Soultz HDR site, *Geophys. J. Int.*, 160, 388-412.
- 11 Evans, K. F., A. Zappone, T. Kraft, N. Deichmann, F. Moia (2012). A survey of the induced
12 seismic responses to fluid injection in geothermal and CO₂ reservoirs in Europe.
13 *Geothermics*, 41, 30– 54.
- 14 Fabriol, H., A. Beauce, A. Genter and R. Jones (1994), Induced microseismicity and its
15 relation with natural fractures: The HDR example of Soultz (France), *Geotherm.*
16 *Resources Council, Trans.*, 18, 423-430.
- 17 Flekkøy, E.G., A. Malthe-Sørenssen, B. Jamtveit, Modeling hydrofracture, *J. Geoph. Res.*
18 (2002), 107, B2151 doi: 10.1029/2000JB000132.
- 19 Garcia, R., G. Natale, M. Monnin, J.L. Seidel (2000), Shock wave radon surface signals
20 associated with the upsurge of T-P solitons in volcanic systems, *J. Vol. Geotherm. Res.*,
21 96(1–2), 15–24.
- 22 Gentier, S., X. Rachez, M. Peter-Borie, and A. Blaisonneau (2011a), Hydraulic stimulation of
23 geothermal wells: Modeling of the hydro-mechanical behavior of a stimulated fractured
24 rock mass, in the proceedings of the XII International Congress of Rock Mechanics,
25 Beijing, China.
- 26 Gentier, S., X. Rachez, M. Peter-Borie, A. Blaisonneau and B. Sanjuan (2011b), Transport
27 and flow modelling of the deep geothermal exchanger between wells and Soultz-sous-
28 Forêts (France), In the proceeding of the Geothermal Resources Council (GRC) annual
29 meeting, San Diego, California.
- 30 Ghani, I., D. Koehn, R. Toussaint, C. W. Passchier (2013), Dynamic development of
31 hydrofracture, *Pure and Applied Geophysics*, in press, 10.1007/s00024-012-0637-7.
- 32 Goren, L., E. Aharonov, D. Sparks and R. Toussaint (2010), The mechanics of pore fluid
33 pressurization in deforming fluid-filled granular material, *J. Geophys. Res.*, 115,
34 B09216, doi:10.1029/2009JB007191

1 Goren, L., E. Aharonov, D. Sparks and R. Toussaint (2011), The Mechanical Coupling of
2 Fluid-Filled Granular Material Under Shear, *P.A. Geoph.* 168, 12, 2289-2323, doi:
3 10.1007/s00024-011-0320-4.

4 Gratier, J. -P., J. Richard, F. Renard, S. Mittempergher, M.L. Doan, G. Di Toro, J. Hadizadeh,
5 and A.M. Boullier (2011), Aseismic sliding of active faults by pressure solution creep:
6 Evidence from the San Andreas Fault Observatory at Depth , *Geology* 39, 12, 1131-
7 1134 , doi:10.1130/G32073.1

8 Gratier, J. -P. (2011), Fault Permeability and Strength Evolution Related to Fracturing and
9 Healing Episodic Processes (Years to Millennia): the Role of Pressure Solution ,*Oil &*
10 *Gas Science and Technology – Revue d’IFP Energies Nouvelles* 66, 3, 491-506 DOI:
11 10.2516/ogst/2010014.

12 Gutenberg, B. and C.F. Richter (1954), *Seismicity of the Earth and Associated Phenomena*,
13 2nd edition, Princeton University Press, Princeton, USA.

14 Hill, D. P., P. A. Reasenber, A. Michael, W. J. Arabaz, G. Beroza, D. Brumbaugh, J. N.
15 Brune, R. Castro, S. Davis, D. de Polo, W. L. Ellsworth, J. Gomberg, S. Harmsen, L.
16 House, S. M. Jackson, M. J. S. Johnston, L. Jones, R. Keller, S. Malone, L. Munguia, S.
17 Nava, J. C. Pechmann, A. Sanford, R. W. Simpson, R. B. Smith, M. Stark, M. Stickney,
18 A. Vidal, S. Walter, V. Wong and J. Zollweg (1993), Seismicity remotely triggered by
19 the magnitude 7.3 Landers, California, earthquake, *Science*, 260, 1617-1623.

20 Huang, H., F. Zhang, P. Callahan, and J. Ayoub (2012a), Fluid Injection Experiments in 2D
21 Porous Media, *SPE Journal*, 17, 3, 903

22 Huang, H., F. Zhang, P. Callahan, and J. Ayoub (2012b), Granular Fingering in Fluid
23 Injection into Dense Granular Media in a Hele-Shaw Cell, *Phys. Rev. Lett.* 108, 258001

24 Ida, Y. (1972), Cohesive force across the tip of a longitudinal-shear crack and Griffith’s
25 specific surface energy, *J. Geophys. Res.*, 77, 3796– 3805.

26 Ide, S. and H. Aochi (2005), Earthquake as multiscal dynamic ruptures with heterogeneous
27 fracture surface energy, *J. Geophys. Res.*, 110, B11303, doi:10.1029/2004JB003591.

28 Ide, S., and M. Takeo (1997), Determination of constitutive relations of fault slip based on
29 seismic wave analysis, *J. Geophys. Res.*, 102(B12), 27379– 27391.

30 Iverson, R.M. (1997), The physics of debris flows, *Rev. Geophys.*, 35, 245-296.

31 Johnsen, Ø., R. Toussaint, K.J. Måløy and E.G. Flekkøy (2006), Pattern formation during
32 central air injection into granular materials confined in a circular Hele-Shaw cell, *Phys.*
33 *Rev. E*, 74, 011301.

- 1 Johnsen, Ø., R. Toussaint, K.J. Måløy, E.G. Flekkøy and J. Schmittbuhl (2007), Coupled
2 air/granular flow in a linear Hele-Shaw cell, *Phys Rev E*, 77, 011301.
- 3 Johnsen, Ø., C. Chevalier, A. Lindner, R. Toussaint, E. Clément, K.J. Måløy, E.G. Flekkøy
4 and J. Schmittbuhl (2008), Decomposition and fluidization of a saturated and confined
5 granular medium by injection of a viscous liquid or a gas, *Phys. Rev. E*, 78, 051302.
- 6 Kaiser, J., *Untersuchungen über das Auftreten von Geräuschen beim Zugversuch* (1950), PhD
7 Thesis, Fak. F. Maschinenwesen, TH München, Germany.
- 8 Kanamori, H. and D. Anderson (1975), Theoretical basis of some empirical relations in
9 seismology, *Bull. Seism. Soc. Am.*, 65, 1073-1095.
- 10 Kanamori, H. and G.S. Stewart (1978). Seismological aspects of the Guatemala earthquake of
11 February 4, 1976, *J. GEophys. Res.*, 83, 3427-3434.
- 12 Kappeimeyer, O., A. Gérard, W. Schloemer, R. Ferrandes, F. Rummel and Y. Benderitter
13 (1991), European HDR project at Soultz-sous-Forêts general presentation, *Geotherm.*
14 *Sci. Tech.*, 2, 263-289.
- 15 Karabulut, H., J. Schmittbuhl, S. Özalaybey, O. Lengliné, A. Kömeç-Mutlu, V. Durand, M.
16 Bouchon, G. Daniel, and M. P. Bouin (2011), *Tectonophysics*, 510, 17-27.
- 17 Kozeny, J. (1927), *Ueber kapillare Leitung des Wassers im Boden*, *Sitzungsber Akad. Wiss.*,
18 *Wien* 136(2a), 271-306.
- 19 Lockner, D.A., Tanaka, H., Ito, H., Ikeda, R., Omura, K., Naka, H. (2009). Geometry of the
20 Nojima fault at Nojima-Hirabayashi, Japan—I. A simple damage structure inferred from
21 borehole core permeability. *Pure Appl. Geophys.* 166, 1649–1667.
- 22 Lombardi, A. M., M. Cocco, and W. Marzocchi (2010), On the increase of background
23 seismicity rate during the 1997-1998 Umbria-Marche, Central Italy, sequence: Apparent
24 variation or fluid-driven triggering?, *Bull. Seism. Soc. Am.*, 100, 1138-1152.
- 25 Løvoll, G., Y. Méheust, R. Toussaint, J. Schmittbuhl and K. J. Måløy (2004), Growth activity
26 during fingering in a porous Hele Shaw cell, *Phys. Rev. E.*, 70, 026301.
- 27 Mai, P. M. and G. C. Beroza (2002), A spatial random field model to characterize complexity
28 in earthquake slip, *J. Geophys. Res.*, 107, 2308, doi:10.1029/2001JB000588.
- 29 Majer, E. L. R. Baria, M. Stark, S. Oates, J. Bommer, B. Smith and H. Asanuma (2007),
30 Induced seismicity associated with enhanced geothermal systems, *Geothermics*, 36,
31 185-222.
- 32 Majer, E., J. Nelson, A. Robertson-Tait, J. Savy and I. Wong (2012), Protocol for addressing
33 induced seismicity associated with enhanced geothermal systems, US Department of
34 Energy, DOE/EE-0662.

1 Matsu'ura, R. S., and I. Karakama (2005), A point-process analysis of the Matsushiro
2 earthquake swarm sequence: The effect of water on earthquake occurrence, *Pure appl.*
3 *Geophys.*, 162, 1319-1345.

4 Mavko, G., T. Mukerli and J. Dvorkin (2009), *The Rock Physics Handbook, Tools for*
5 *Seismic Analysis of Porous Media*, 2nd edition, Cambridge University Press.

6 Mazzoldi A., A. P. Rinaldi, A. Borgia and J. Rutqvist (2012). Induced seismicity within
7 geologic carbon sequestration projects: Maximum earthquake magnitude and leakage
8 potential. *International Journal of Greenhouse Gas Control*, 10, 434–442.

9 Miller, S. A., C. Collettini, L. Chiaraluce, M. Cocco, M. Barchi and B. J. P. Kaus (2004),
10 Aftershocks driven by a high-pressure CO₂ source at depth, *Nature*, 427, 724-727.

11 Miller, S. A. and A. Nur (2000), Permeability as a toggle switch in fluid-controlled crustal
12 processes, *Earth Planet. Sci. Lett.*, 183, 133-146.

13 Miller, S., A. Nur and D. Olgaard (1996), Earthquakes as a coupled shear stress-high pore
14 pressure dynamical system, *Geophys. Res. Lett.*, 23, 197, 200.

15 Nakatani, M. (1997), Experimental study of time-dependent phenomena in frictional faults as
16 a manifestation of stress-dependent thermally activated process, Ph.D. Thesis, The
17 University of Tokyo.

18 Neuville, A., R. Toussaint and J. Schmittbuhl (2009), Fracture roughness and thermal
19 exchange: a case study at Soultz-sous-Forets, *C.R.A.S. Geoscience*, 342, 616.
20 doi:10.1016/j.crte.2009.03.006

21 Niebling, M.J., E.G. Flekkøy, K.J. Måløy, R. Toussaint (2010a), Sedimentation instabilities:
22 impact of the fluid compressibility and viscosity, *Phys. Rev. E* 82, 051302. doi:
23 10.1103/PhysRevE.82.051302.

24 Niebling, M.J., E.G. Flekkøy, K.J. Måløy, R. Toussaint (2010b), Mixing of a granular layer
25 falling through a fluid, *Phys. Rev. E* 82, 011301.

26 Niebling, M., R. Toussaint, E.G. Flekkøy and K.J. Måløy (2012a), Estudios numéricos de
27 Aerofractures en medios poros / Numerical Studies of Aerofractures in Porous Media,
28 *Revista Cubana de Física*, 29, 1E, 1E66.

29 Niebling, M.J., R. Toussaint, E.G. Flekkøy, K.J. Måløy (2012b), Dynamic aerofracture of
30 dense granular packings, *Phys. Rev. E*, 86, 061315.

31 Nur, A. And J.D. Byerlee (1971), An exact effective stress law for elastic deformation of rock
32 with fluids. *J. Geophys. Res.*, 76(26):6414–6419.

33 Obara, K. (2002), Nonvolcanic deep tremor associated with subduction in southwest Japan,
34 *Science*, 296, 1679-1681.

- 1 O'Connell, R. J. and B. Budiansky (1974), Seismic velocities in dry and saturated cracked
2 solids, *J. Geophys. Res.*, 79, 5412-5426.
- 3 Ohnaka, M. (2003), A constitutive scaling law and a unified comprehension for frictional slip
4 failure, shear fracture of intact rock, and earthquake rupture, *J. Geophys. Res.*, 108(B2),
5 2080, doi:10.1029/2000JB000123.
- 6 Ohtake, M. (1976), A review of the Matsushiro earthquake swarm, *Kagaku*, 46, 306-313 (in
7 Japanese).
- 8 Palmer A. C., and J. R. Rice (1973), The growth of slip surfaces in the progressive failure of
9 over-consolidated clay, *Proc. R. Soc. London, Ser. A*, 332, 527-548.
- 10 Perfettini, H., J. Schmittbuhl, and J.P. Vilotte (2001). Slip correlations on a creeping fault.
11 *Geophys. Res. Lett.*, 28(10):2137-2140.
- 12 Person, C (1981), The relationship between microseismicity and high pore pressure during
13 hydraulic stimulation experiments in low permeability granite rocks, *J. Geophys. Res.*,
14 86, 7855-7864.
- 15 Revil, A. (2002), Genesis of mud volcanoes in sedimentary basins : A solitary wave-based
16 mechanism, *Geophysical Research Letters*, 29,12, 10.1029/2001GL014465.
- 17 Rice, J. R. (1993), Spatio-temporal complexity of slip on a fault, *J. Geophys. Res.*, 98, 9885-
18 9907.
- 19 Rice, J. R. (2006), Heating and weakening of faults during earthquake slip, *J. Geophys. Res.*,
20 111, B05311, doi:10.1029/2005JB004006.
- 21 Rozhko, A.Y. (2010), Role of seepage forces on seismicity triggering, *J. Geophys. Res.*, 115,
22 B11314, doi:10.1029/2009JB007182.
- 23 Schelstraete, M. (2009), Suivi de la décompaction et aérofracturation de matériaux faiblement
24 consolidés, Masters thesis, University of Strasbourg, France.
- 25 Schmittbuhl, J., J.P. Vilotte, and S. Roux (1993). Propagative macrodislocation modes in an
26 earthquake fault model. *Europhys. Lett.*, 21:375-380.
- 27 Schmittbuhl, J., G. Chambon, A. Hansen and M. Bouchon (2006), Are stress distributions
28 along faults the signature of asperity squeeze?, *Geophys. Res. Lett.*, 33, L3307,
29 doi:10.1029/2006GL025952.
- 30 Segall, P. and J. R. Rice (1995), Dilatancy, compaction and slip instability of a fluid-
31 infiltrated fault, *J. Geophys. Res.*, 100, 22155-22171.
- 32 Segall, P. and J. R. Rice (2006), Does shear heating of pore fluid contribute to earthquake
33 nucleation?, *J. Geophys. Res.*, 111, B09316, doi:10.1029/2005JB004129.

- 1 Shapiro, S. A., P. Audigane and J.-J. Royer (1999), Large-scale in situ permeability tensor of
2 rocks from induced microseismicity, *Geophys. J. Int.*, 137, 207-213.
- 3 Shapiro, S. A. and C. Dinske (2009), Fluid-induced seismicity: Pressure diffusion and
4 hydraulic fracturing, *Geophys. Pros.*, 57, 301-310.
- 5 Tada, T., E. Fukuyama and R. Madariaga (2000), Non-hypersingular boundary integral
6 equations for 3-D non-planar crack dynamics, *Comput. Mech.*, 25, 613– 626.
- 7 Terakawa, T., A. Zoporowski, B. Galvan and S. A. Miller (2010), High-pressure fluid at
8 hypocentral depths in the L’Aquila region inferred from earthquake focal mechanisms,
9 *Geology*, 38, 995-998.
- 10 Terzaghi, K. (1943), *Theoretical soil mechanics*, John Wiley and Sons, New York.
- 11 Thurber, C., S. Roecker, W. Ellsworth, Y. Chen, W. Lutter and R. Sessions (1997), Two-
12 dimensional seismic image of the San Andreas fault in the northern Gabilan range,
13 central California: Evidence for fluids in the fault zone, *Geophys. Res. Lett.*, 24, 1591-
14 1594.
- 15 Vinningland, J.L., Ø Johnsen, E.G. Flekkøy, R. Toussaint and K.J. Måløy (2007a), A granular
16 Rayleigh-Taylor instability: experiments and simulations, *Phys. Rev. Lett.*, 99, 048001.
- 17 Vinningland, J.L., Ø. Johnsen, E.G. Flekkøy, R. Toussaint and K.J. Måløy (2007b),
18 Experiments and Simulations of a gravitational granular flow instability, *Phys. Rev. E*,
19 76, 051306.
- 20 Vinningland, J.L., Ø. Johnsen, E.G. Flekkøy, R. Toussaint and K.J. Måløy (2010), Influence
21 of particle size in Rayleigh Taylor granular flow instability, *Phys. Rev. E* 81, 041308.
- 22 Vinningland, J.L., R. Toussaint, M. Niebling, E.G. Flekkøy and K.J. Måløy (2012), Family-
23 Vicsek scaling of detachment fronts in Granular Rayleigh Taylor Instabilities during
24 sedimenting granular/fluid flows, *European Physics Journal-Special Topics*, 204, 1, 27-
25 40. doi: 10.1140/epjst/e2012-01550-2
- 26 Walder, J. and A. Nur (1984), Porosity reduction and crustal pore pressure development, *J.*
27 *Geophys. Res.*, 89, 11539-11548.
- 28 Wong, T.-F., S.-C. Ko and D. L. Olgaard (1997), Generation and maintenance of pore
29 pressure excess in a dehydrating system, 2. Theoretical analysis, *J. Geophys. Res.*, 102,
30 841-852.
- 31 Yamashita, T. (1999), [Pore creation due to fault slip in a fluid-permeated fault zone and its
32 effect on seismicity, *Pure Appl. Geophys.*, 155, 625-647.](#)
- 33 Zimmerman, R. W. and G. S. Bodvarsson (1996), Effective transmissivity of a two-
34 dimensional fracture network, *Int. J. Rock Mechanics*, 33, 433-438.

1 Zimmerman, R. W. and I.G. Main (2004),, Hydromechanical behaviour of fractured rocks,
 2 *In:Mechanics of Fluid-Saturated Rocks, Ed. Y. Gueguen and M. Bouteca*, London and
 3 San Diego, Academic Press, 363-421,

4 Zoback, M. D. and S. M. Gorelick (2012), Earthquake triggering and large scale geologic
 5 storage of carbon dioxide, Proc. Natl. Acad. Sci. U.S.A., doi:10.1073/pnas.1202473109.

6
 7
 8
 9

10 **Appendix 1: Elastic equation for stress redistribution**

11 The theory of the linear static elasticity gives us a unique solution based on the
 12 equilibrium theory. The stress change at any place in the medium is written as a convolution
 13 of the causal fault slip over and the response function (Green function), G , over the whole
 14 area of the fault (Σ):

$$15 \quad \Delta\tau(\vec{x}) = \int_{\Sigma} G(\vec{x}-\vec{\xi})\Delta u(\vec{\xi})d\Sigma. \quad (A1)$$

16 The response function G has symmetry with respect to the relative location $(\vec{x}-\vec{\xi})$. Let us
 17 discuss only on a fault plane ($z = 0$) and discretize (x, y) -fault plane in squares of the equal
 18 size; $\vec{x} = (i\Delta s, j\Delta s, 0)$ and $\vec{\xi} = (l\Delta s, m\Delta s, 0)$. Then we can write (A1) as

$$19 \quad \Delta\tau_{ij} = \sum_{l,m} G_{(i-l)(j-m)}\Delta u_{lm}. \quad (A2)$$

20 Tada et al. (2000) provide the analytical solution for the 3D homogeneous, elastic, isotropic
 21 medium. For a dislocation in the x -direction, shear stress in xz -component is written as

$$22 \quad \Delta\tau(\vec{x}) = -\frac{\mu}{4\pi} \int_{\Sigma} d\Sigma \left[2(1-p^2) \frac{\gamma_1}{r^2} \frac{\partial\Delta u}{\partial x} + \frac{\gamma_2}{r^2} \frac{\partial\Delta u}{\partial y} \right] \quad (A3)$$

23 where $p^2 = \beta^2 / \alpha^2$ (α : P-wave velocity, β : S-wave velocity), $r^2 = |\vec{x}-\vec{\xi}|^2$ and
 24 $\gamma_i = (x_i - \xi_i) / r$. In such boundary integral equation formulations, slip on an element is
 25 usually assumed uniform;

$$\begin{aligned}
\Delta u(\vec{\xi}) = \Delta u_m & \left[H(\xi_1 - (l-1/2)\Delta s)H(\xi_2 - (m-1/2)\Delta s) \right. \\
& - H(\xi_1 - (l-1/2)\Delta s)H(\xi_2 - (m+1/2)\Delta s) \\
& - H(\xi_1 - (l+1/2)\Delta s)H(\xi_2 - (m-1/2)\Delta s) \\
& \left. + H(\xi_1 - (l+1/2)\Delta s)H(\xi_2 - (m+1/2)\Delta s) \right]
\end{aligned} \tag{A4}$$

and we estimate the stress at the center of each element $(i\Delta s, j\Delta s)$. We can obtain the analytical solution from (A3) for a unit slip $\Delta u = \Delta u \cdot H(x_1)H(x_2)$;

$$\Delta \tau(\vec{x}) = -\frac{\mu \Delta u}{4\pi} \left[\frac{1}{\sqrt{x_1^2 + x_2^2}} \left\{ 2(1-p^2) \frac{x_2}{x_1} + \frac{x_1}{x_2} \right\} - \left\{ 2(1-p^2) \frac{1}{x_1} + \frac{1}{x_2} \right\} \right]. \tag{A5}$$

Consequently, we can obtain the response function for Equation (A4) by combining the solution (A5), as illustrated in Figure A1. Note that the stress remains finite at any collocation points, including on the causal source element $(0, 0)$ and the neighbouring elements $(\pm 1, \pm 1)$. The detailed derivation of the equations is given in Tada et al. (2000).

Appendix 2: Resolution in numerical simulations

In the overall study, we suppose an element size of 30 m, which allows a minimum earthquake of about M1.3 under the given friction law, namely, Equation (16). As the system of the equations is a highly nonlinear self-organising system, we are concerned about the resolution of the numerical simulations seen at different scales. Figure A2 represents a simulation with a grid size of 50 m (time step of 2 s) for the same physical parameters used in Figure 4. As expected the minimum magnitude appearing during the simulation increases to about 1.8, namely smaller earthquakes than this are not modelled. Consequently, the number of earthquakes decreases. Due to the nonlinearity and different discretization, we may not find the same earthquake (epicentre location, magnitude, time, etc.) in a deterministic manner, strictly speaking. However the statistical features of the seismicity is the same. The seismicity propagates outwards and then we find a maximum event of Mw 4.47 at 4.9 hours after the injection start (previously Mw 4.52 at 4.1 hour in Figure 4). Most of the seismicity is calmed after 6 hours. The pore pressures on the fault (lines in red and orange) show an identical behaviour at different points. These observations assure the coherence in our discussions on the statistical characters of the seismicity evolution and fluid circulation.

On the other hand, one may also pose a question about the slip-weakening distance (D_c) used in this study. We dare to take it very small, because we do not want to bring any

1 complex discussion about its temporal evolution (e.g. Nakatani 1997; Aochi and Matsu'ura,
2 2002) or its scaling problem (e.g. Ohnaka, 2003; Aochi and Ide, 2009). However it is worth
3 mentioning what may happen if we take a longer D_c . The fact of small D_c is that the rupture
4 brings the totality of the stress drop described by Equation (15) regardless of the dimension of
5 rupture (number of ruptured elements). This is why the smallest earthquakes are aligned
6 around a magnitude 1.3. Later on, smaller earthquakes appear, because an increase in the pore
7 pressure leads to a decrease in effective normal stress and consequently a smaller stress drop.

8 Figure A3 represents a simulation assuming $D_c = 0.01$ [m] under the same
9 configuration with Figure 4. We note that $D_c = 0.01$ [m] is a reasonable value for an event of
10 magnitude 4 (Ohnaka 2003; Ide and Aochi, 2005). A long D_c allows a tiny displacement with
11 a smaller stress drop (a very small magnitude event), and this generates only a slight stress
12 concentration in the surrounding (schematic illustration in Figure A4). In order to accumulate
13 enough shear stress in the surrounding, many small earthquakes are required. On the other
14 hand, as described in Equation (19), the permeability becomes immediately large once the
15 concerned element is ruptured regardless of its slip amount. Thus, the fluid circulation may
16 later on play a role in reducing the fault strength during the seismicity. As a result, the
17 seismicity appearance becomes very complex, and their magnitude-frequency relation is not
18 any more a continuous linear inverse relation. Taking into account a finite length of D_c is
19 required particularly when considering a certain pre-fixed size of earthquake and its
20 preparation process (e.g. towards a M4 event in this case), however this does not assure the
21 self-organizing system of multi-scale phenomena. For this purpose, ones will have to carry
22 out dynamic rupture simulations taking into account of the inertia and scaling problem (e.g;
23 Aochi and Ide, 2009). However for the purpose of this study and for the simplicity of the later
24 discussion, we adopt the assumption that D_c is small enough to let the complete stress drop
25 every time.

26

27 **Appendix 3: Preliminary attempt on fault evolution**

28 As our preliminary attempt, we have tested the continuous, relatively gentle, relations,
29 Equations (17) and (18). In Figure A5, we show two test cases in the first twelve hours during
30 the continuous injection, supposing $u_c = 0.01$ m in Equation (17) and $n = 5$ or 10 in Equation
31 (18). The porosity and the permeability are shown for the central element where the fluid is

1 injected. In both cases, the system finds rapidly the equilibrium status (fluid circulates) after
2 only a few events without any significant seismicity. As observed in the lower panels, the
3 permeability and the porosity changes are so quick, and practically discontinuous, and are
4 also saturated, as the porosity is forced to be limited to 0.45, although this sounds extremely
5 large. As the rupture process is nonlinear, the slip amount of successive events differ from
6 each other are very difficult to control, while the relations such as Equations (17) and (18) are
7 unique. These examples show the difficulty to control the fluid circulation in simple equations.
8 Thus we will adopt a discontinuous phase change in permeability change according to the
9 rupturing.
10

1 Table 1: Model parameters

Parameter	Quantity
Element size Δs	30 m
Time step Δt	1 s
Fluid viscosity η	2×10^{-4} Pa.s
Fluid density ρ	1×10^3 kg/m ³
Fluid compressibility $\beta_{f\phi}$	5×10^{-10} Pa ⁻¹
Elastic medium compressibility β_ϕ	5×10^{-11} Pa ⁻¹
Injection rate Γ	31.5 [l/s] during the first 24 hours
Rigidity of elastic medium μ	30 GPa
Normal stress (confining pressure) σ_n	100 MPa
Background pore pressure	30 MPa
Static friction coefficient μ_f, μ_f'	0.65 (for the first rupture), 0.6 (for the rest)
Dynamic friction coefficient μ_d	0.55
Critical slip displacement D_c	< 0.001 cm

2

3 Table 2: Three fault parameters in the first examples.

Parameter	Initial value	Evolution allowed
Fault width h	1, 3 or 5 m	Variable
Permeability κ	10^{-13} m ²	Invariable, const
Porosity ϕ	0.05	Variable only by elastic change

4

5

6

1 Figure captions

2 Figure 1: Conceptual illustration of fault internal structure (after Chester et al., 1994) and our
3 model allowing fluid circulation and induced seismicity predominantly along a
4 preexisting 2D fault plane with a fault core of width $h(x, y)$. The fault core is
5 surrounded by impermeable rock. Fault slip is given by $\Delta u(x, y)$ directed along the x -
6 axis, so that the shear stress $\tau(x, y)$ of interest is a xz -component. The pore pressure in
7 the fault core $P(x, y)$ can evolve due to the injection $\Gamma(x, y)$, as a function of the
8 variable fault constitutive parameters of porosity $\phi(x, y)$ and permeability $\kappa(x, y)$.

9 Figure 2: Numerical algorithm used in this study. In the left hand side, the loop is concerned
10 about the fluid circulation. Once the rupture criterion is reached (left bottom), the
11 rupture process is solved at the right hand side. Every time, fault property (porosity and
12 permeability) may evolve.

13 Figure 3: Simulated seismicity versus time in the case of invariable permeability ($\kappa = 10^{-13}$
14 m^2) for different initial fault widths (h_0) of 1, 3 and 5 m, in (A) model H1, (B) model H3
15 and (C) model H5, respectively. The seismicity is plotted by dots, colored to reflect the
16 epicentral distance from the injection point, and the number of earthquakes per hour is
17 also shown in the form of histograms. The injection rate is indicated by blue lines. The
18 pore pressure, represented by red and orange curves, corresponds to two different spots,
19 the injection point $(x, y) = (1500 \text{ m}, 1500 \text{ m})$ and another point $(1290 \text{ m}, 1290 \text{ m})$,
20 respectively; their position is indicated by triangles in a snapshot (cumulative slip, pore
21 pressure, permeability and shear stress) at time $t = 80,000 \text{ sec}$, indicated by a line (1).

22 Figure 4: Simulated seismicity with variable permeability. Hereafter it is referred as model K2.
23 Snapshots are shown at two different times, labeled (1) and (2). See also the caption for
24 Figure 3.

25 Figure 5: Simulated seismicity for two heterogeneous fields of initial shear stress, (A) model
26 K2_SH10: $\delta = 0.1$ (i.e., 10 %) and (B) model K2_SH20: 0.2 (20 %). Snapshots are
27 shown at two different times, labeled (1) and (2). See also the caption for Figure 3.

28 Figure 6: Simulated seismicity for two descriptions of heterogeneous fault strengths, (A)
29 model K2_TC20: spatially continuous and (B) model K2_TD20: discontinuous cases.
30 Snapshots are shown at two different times labeled (1) and (2). See also the caption for
31 Figure 3.

32 Figure 7: The magnitude-frequency relations for different simulations. The first panel shows
33 four different cases of heterogeneous initial shear stress field, model K2 (Figure 3),

1 K2_ST10 (Figure 4(A)), K2_ST20 (Figure 4(B)) and K2_ST30 with $\delta = 0.3$ (30 %). The
2 second panel shows the cases of different wavelengths based on K2_ST20.

3 Figure 8: Simulated seismicities for short injection durations. (A) Model K2_I3: three hours of
4 injection for the homogeneous condition (the same configuration as model K2 in Figure
5 4), and (B) model K2_ST20_I4: four hours of injection for heterogeneous condition (cf.
6 model K2_ST20 in Figure 5). The latter case requires a longer injection because the
7 initial shear stress at the injection point happens to be low.

8 Figure 9: Simulated seismicity for the case of $\beta = 1/(21,600 \text{ s})$, model K2_B6, for an
9 injection of 24 hours (the same as Figure 4 except for β).

10 Figure 10: Simulation results for the cases of $\beta = 1/(3600 \text{ s})$ for a short injection duration.
11 (A) Model K2_B1: homogeneous and (B) model K2_SH20_B1: heterogeneous initial
12 shear stresses are given, respectively, letting $\lambda_x = \lambda_y = 300 \text{ m}$. Snapshots are shown for
13 the two different moments for each simulation. In the latter case, the pore pressure is
14 trapped after injection has stopped and the fault is not entirely ruptured.

15 Figure 11: Evolution of seismicity according to varied injection rate with time (model SB).
16 The stress redistribution affects only the adjacent elements and the permeability changes
17 evolutionally every event.

18 Figure 12: Evolution of seismicity for the four cases in time-versus-distance graphs, models
19 K2 (Figure 4), K2_SH20_I4 (Figure 7(B)), K2_B6 (Figure 9) and K2_SH20_B1 (Figure
20 10(B)). The injection rate is shown by grey lines. The dots (individual earthquakes) are
21 color-coded for magnitude.

22 Figure A1: Shear stress redistribution in the 3D homogeneous elastic medium due to a
23 dislocation (slip direction is parallel to the x-axis) located at the center of the fault plane.
24 All the axes are normalized.

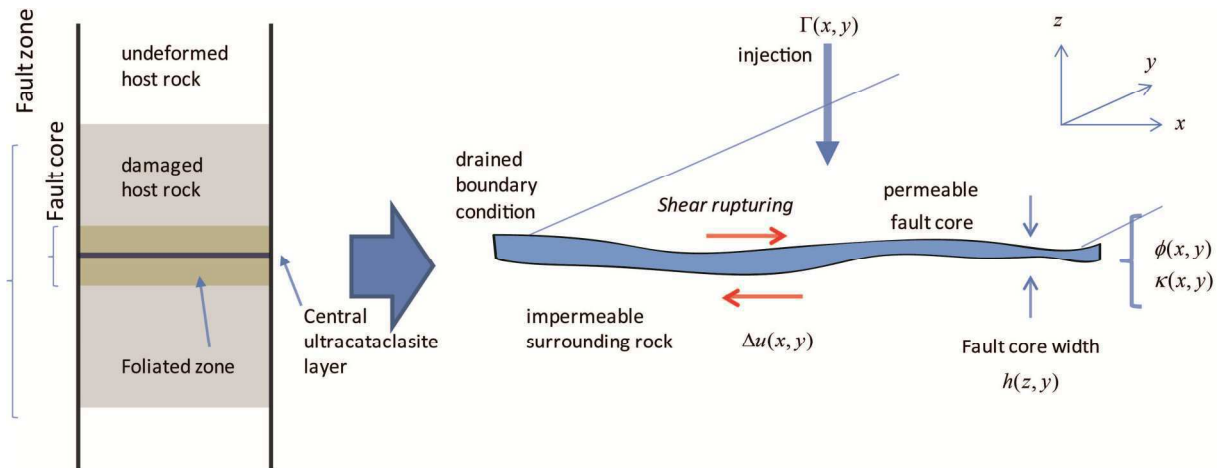
25 Figure A2: The same situation as model K2 in Figure 4 but with an element size of 50 m for
26 checking the numerical resolution. The statistical feature of the appearing seismicity and
27 the fluid circulation are consistent in the both simulations. For notations, see also the
28 caption for Figure 3.

29 Figure A4: The same situation as model K2 in Figure 4 but with a critical slip displacement
30 D_c of 0.01 m.

31 Figure A3: A schematic illustration of the stress release and redistribution in the cases of (1)
32 immediate stress drop (D_c small enough) and (2) a longer D_c . As illustrated at the top
33 corner, the slope (grey line) of the relaxation is determined by the system of the elastic

1 equations. The discrepancy between the charged shear stress and the fault strength is
2 equilibrated by an increment slip. Namely the equilibrium state is the cross between the
3 relaxation line (solid grey) and the friction lines (dotted or broken lines). If D_c is small
4 enough, frictional slope is steeper than the grey line, so that the system always finds the
5 equilibrium state at the residual level of friction, as line (1). Besides, when D_c is large
6 enough such as case (2), the equilibrium state is found with a small amount of stress
7 drop and fault slip. As a result, stress concentration in the surrounding is large in case
8 (1) comparing to case (2). However the fault character evolves independently from the
9 fault slip and stress drop in Equation (17).
10

1 Figure 1: Sketch of the fault core model.

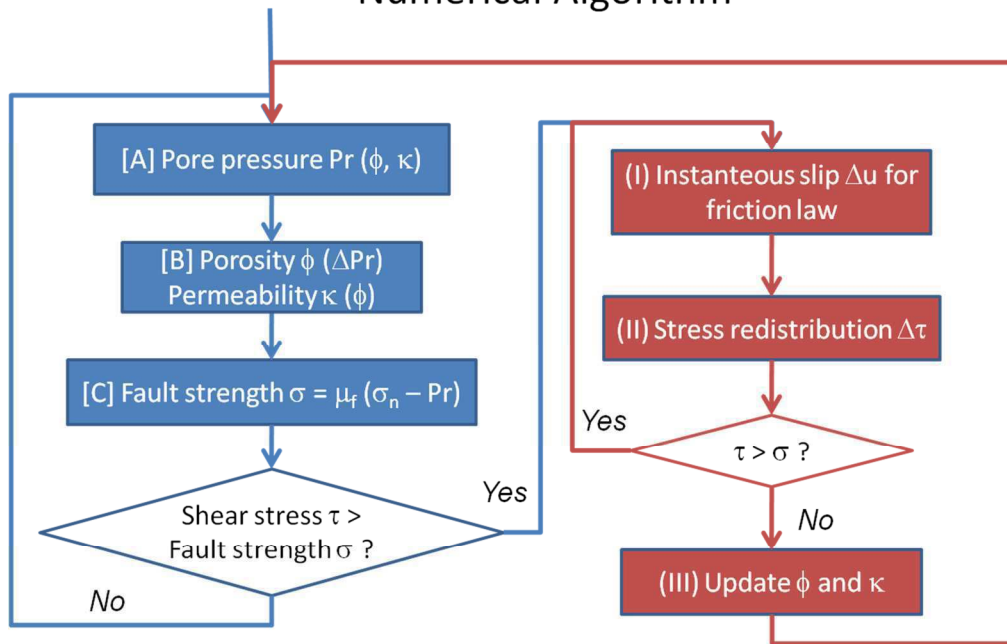


2 modified after Chester et al. (1993)

3

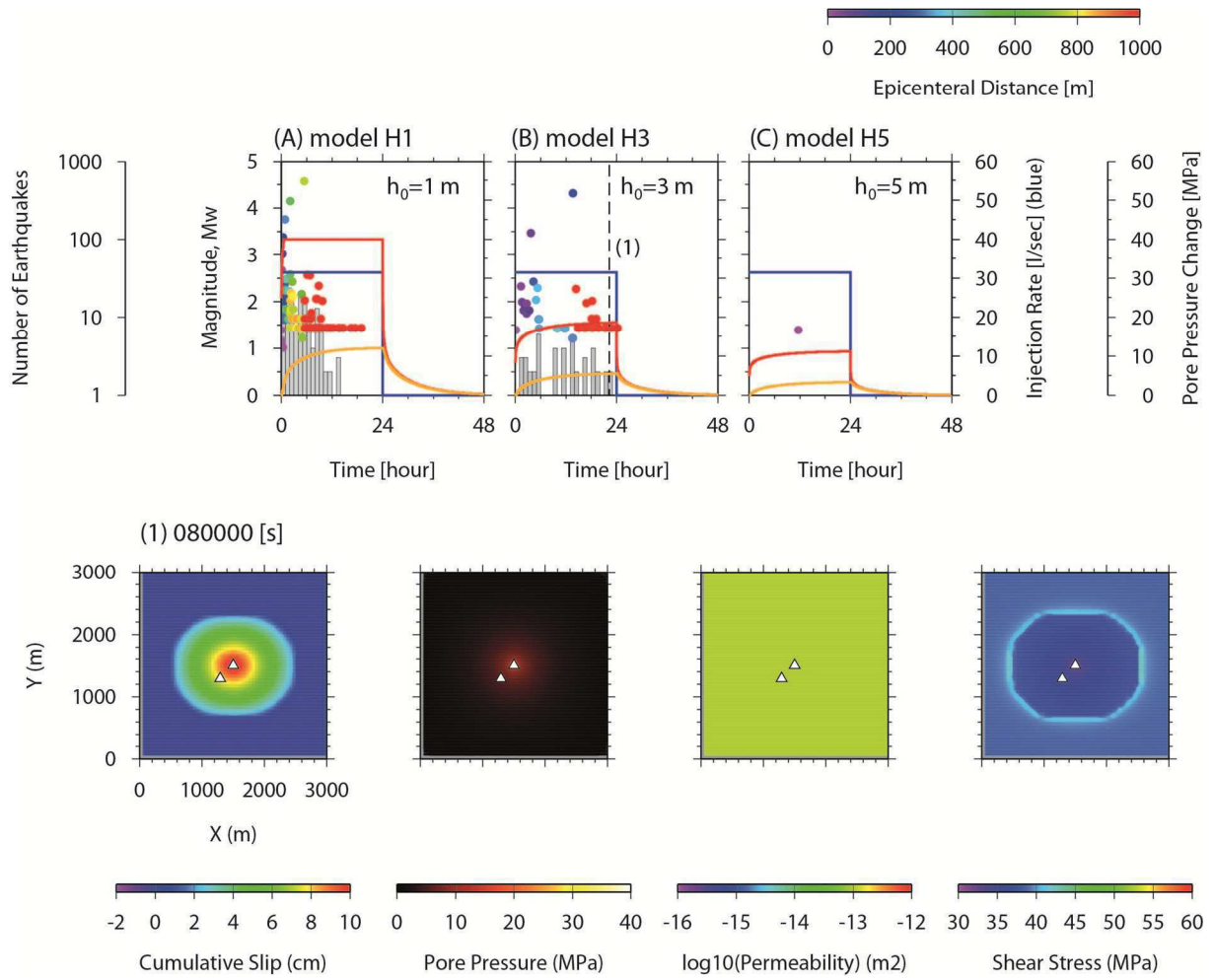
1 Figure 2 :

Numerical Algorithm



2

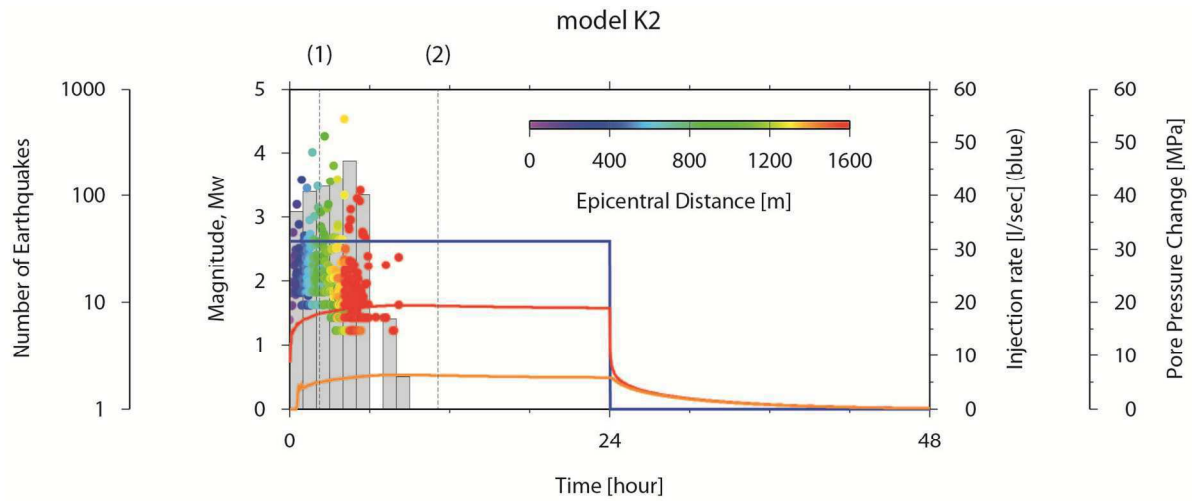
1 Figure 3:



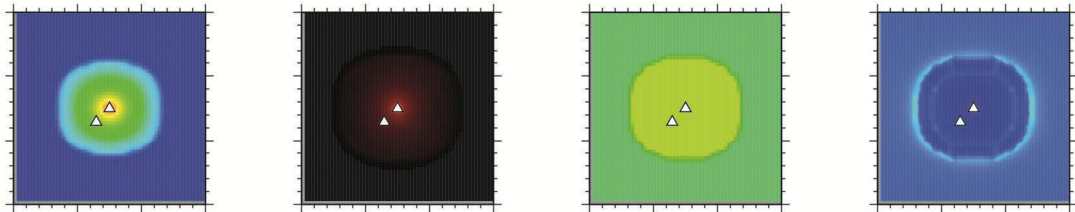
2

3

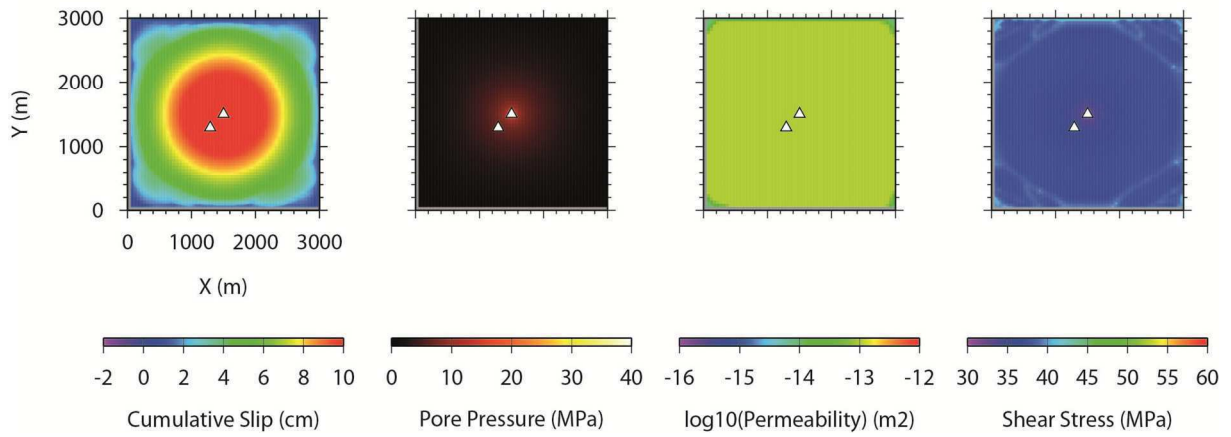
1 Figure 4:



(1) 008000 [s]



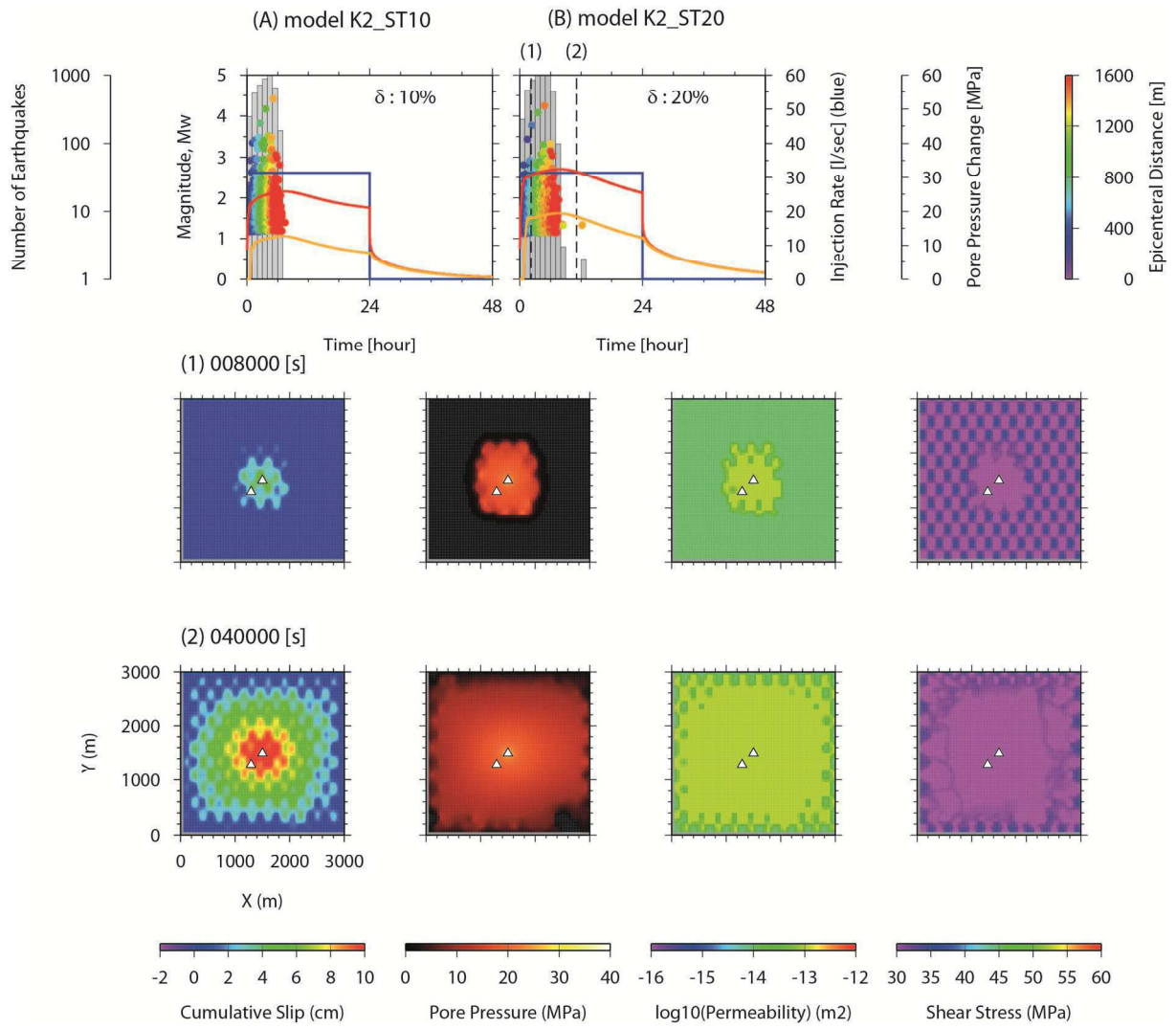
(2) 040000 [s]



2

3

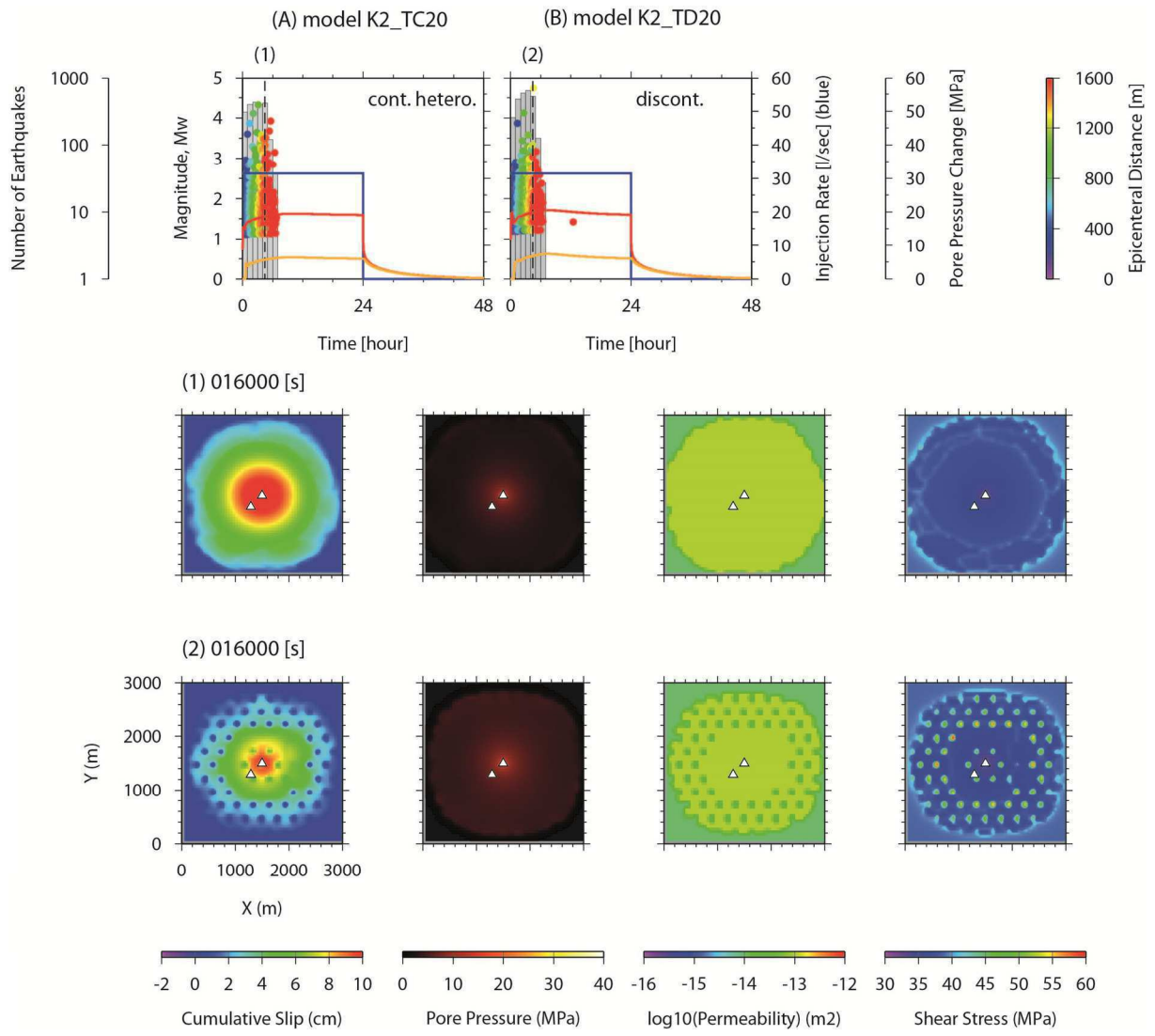
1 Figure 5:



2

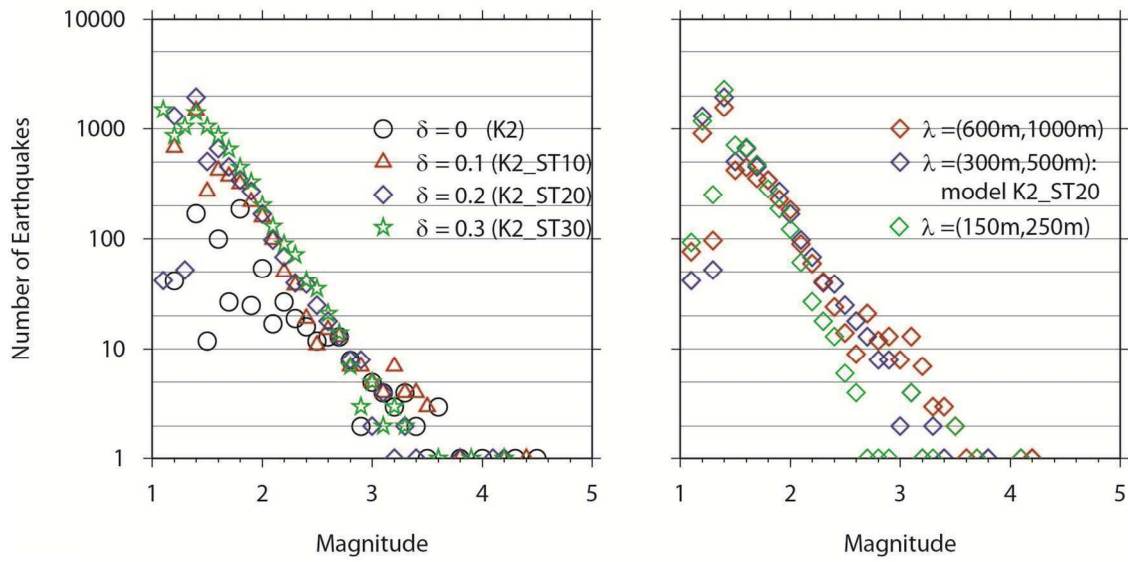
3

1 Figure 6:

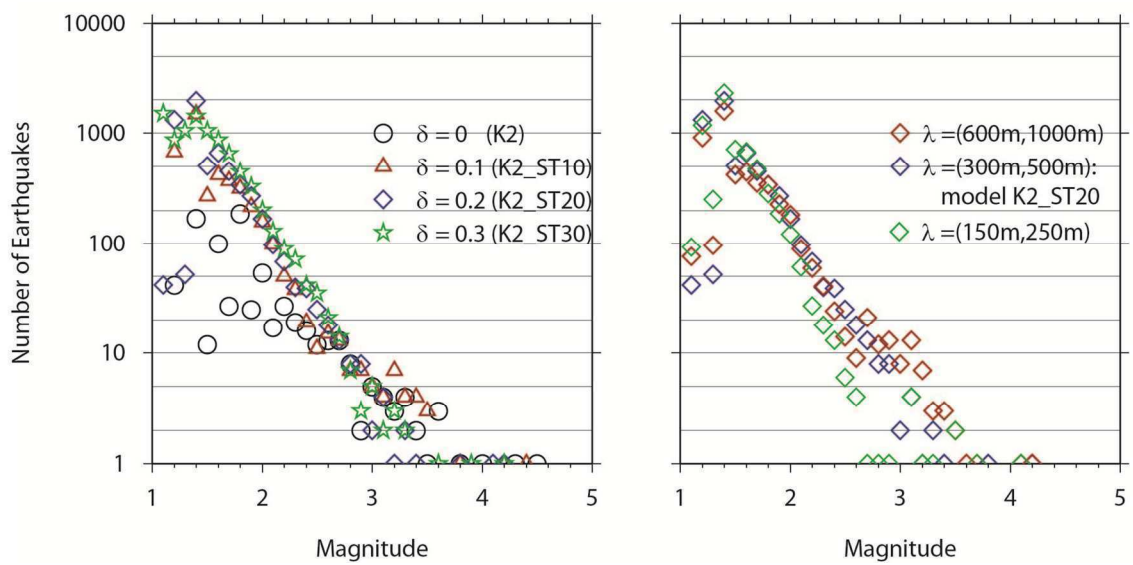


2
3

1 Figure 7:



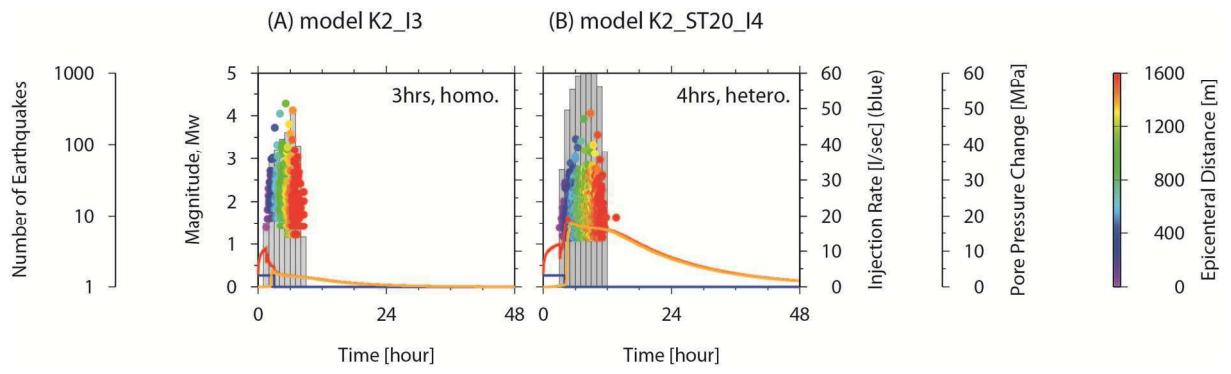
2



3

4

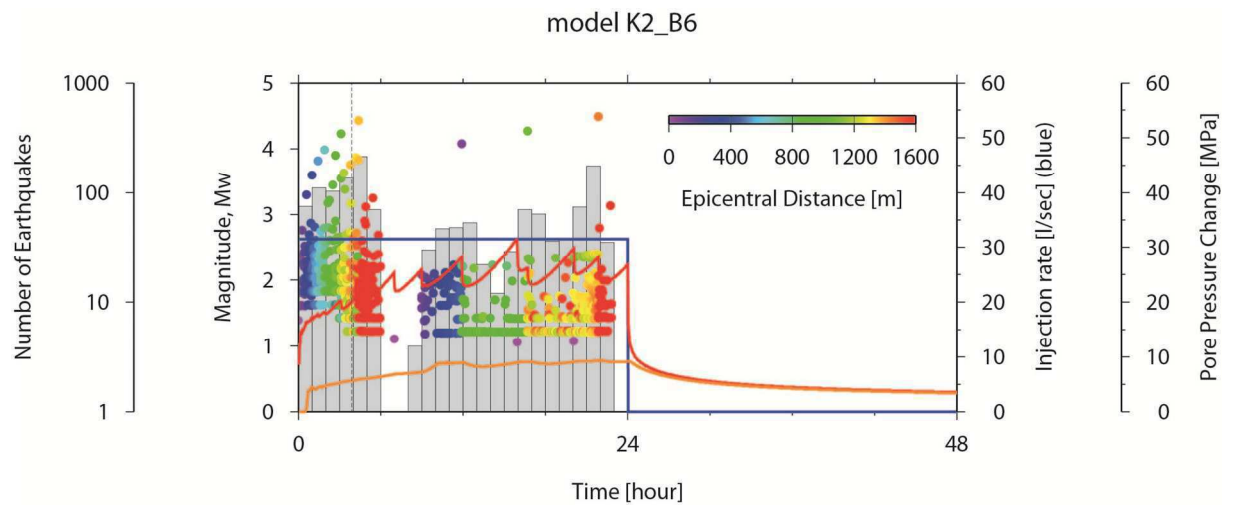
1 Figure8:



2

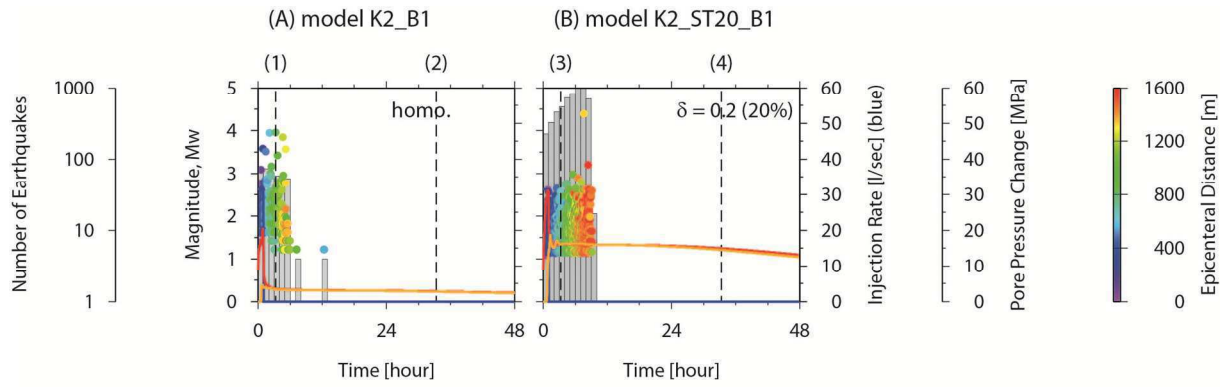
3

1 Figure 9:

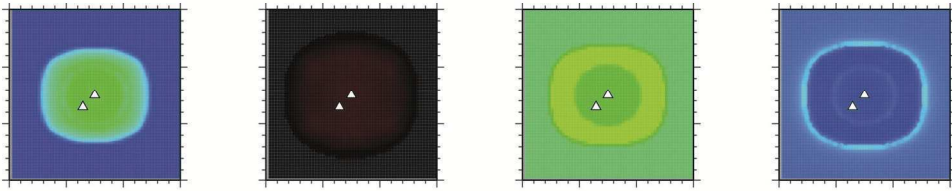


2
3

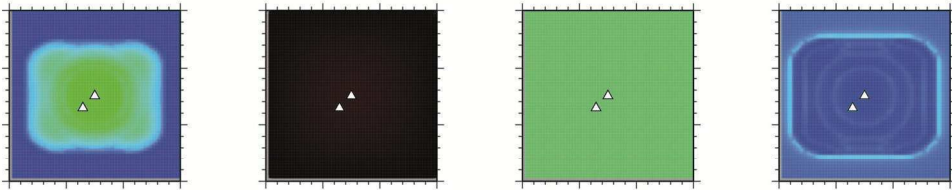
1 Figure 10:



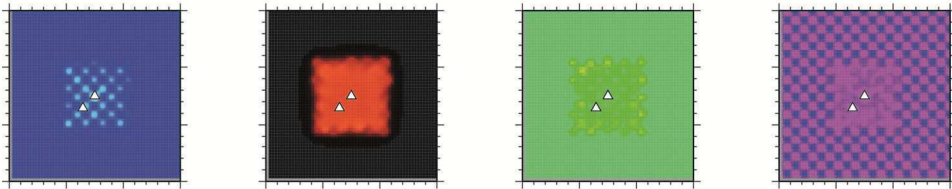
(1) homogeneous initial shear stress, $t=012000$ [s]



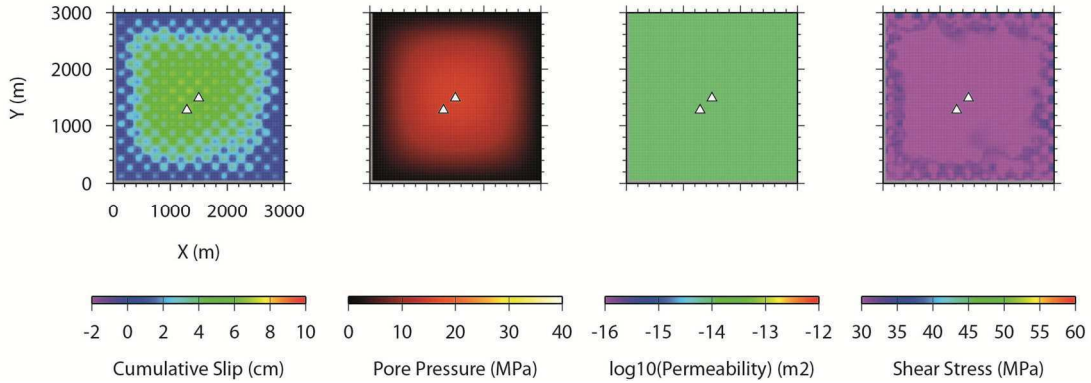
(2) homogeneous initial shear stress, $t=120000$ [s]



(3) heterogeneous (δ 20%), $t=012000$ [s]



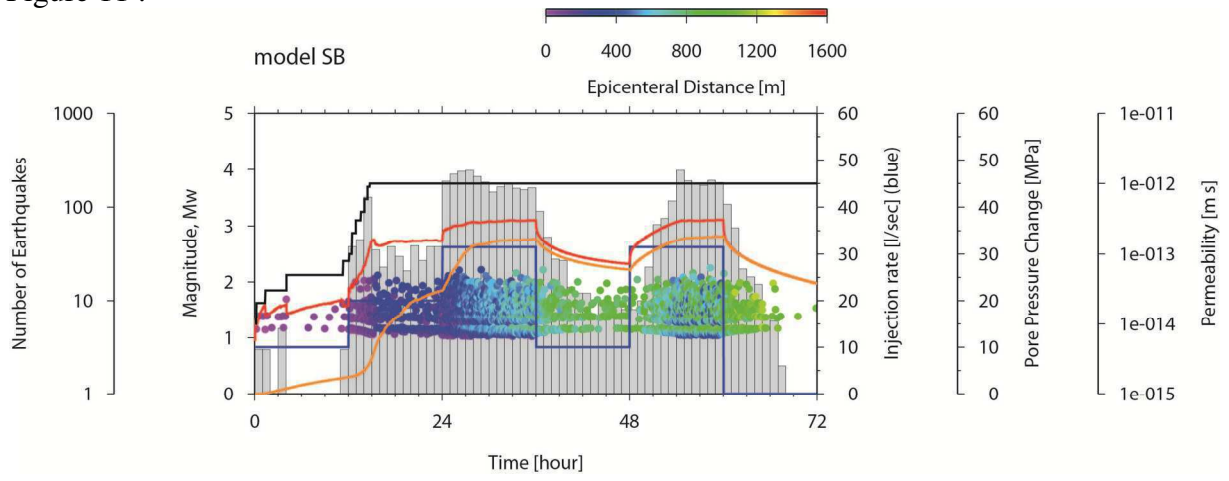
(4) heterogeneous (δ 20%), $t=120000$ [s]



2

3

1 Figure 11 :

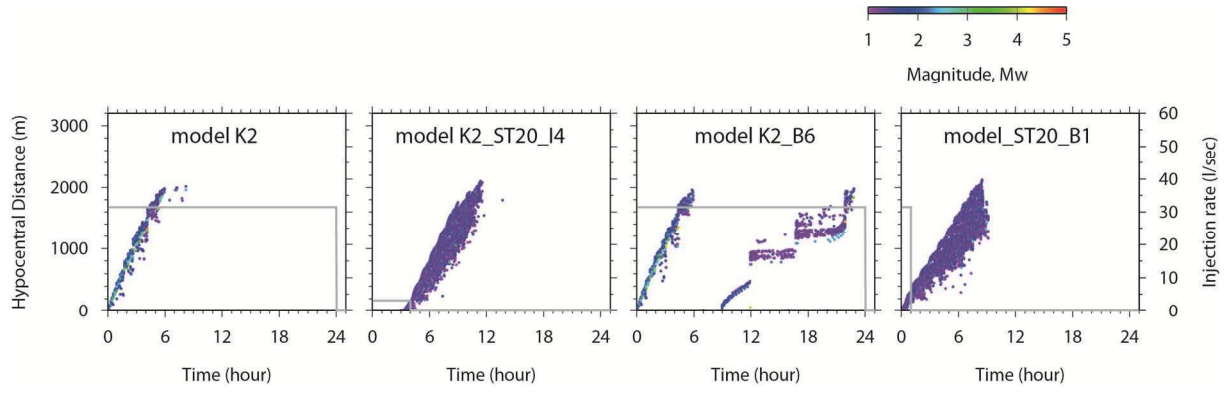


2

3

1

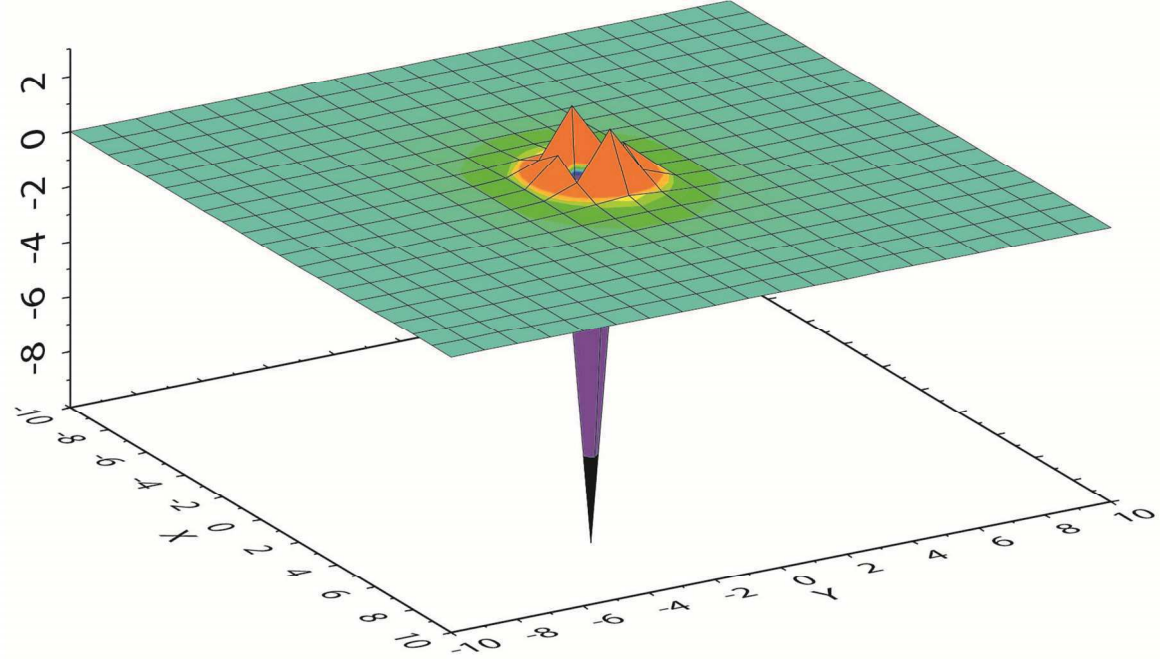
2 Figure 12 :



3

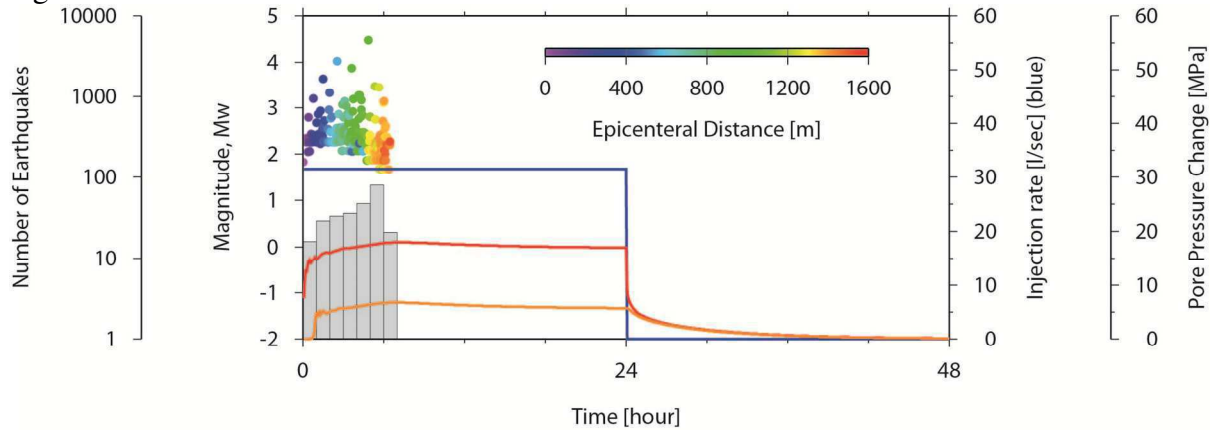
4

1
2 Figure A1 :



3
4

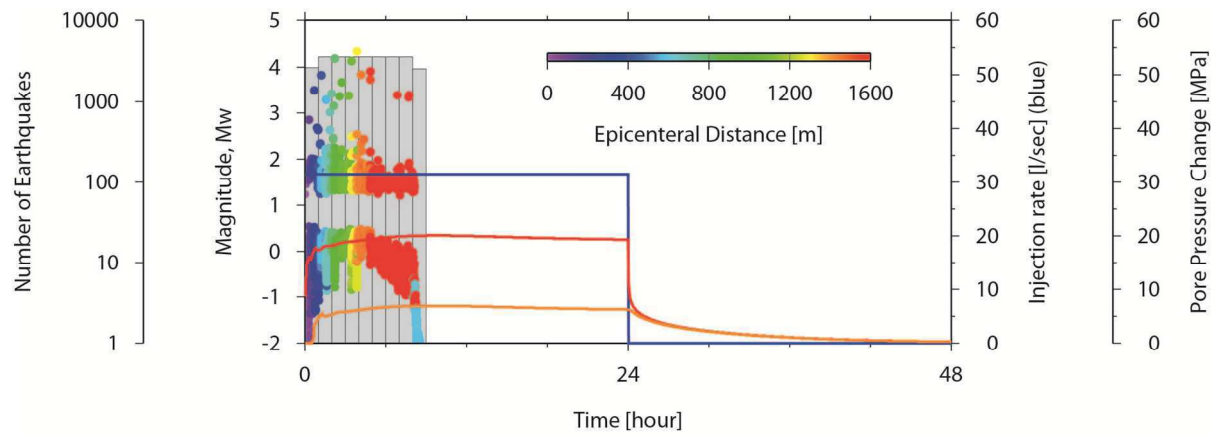
1 Figure A2



2

3

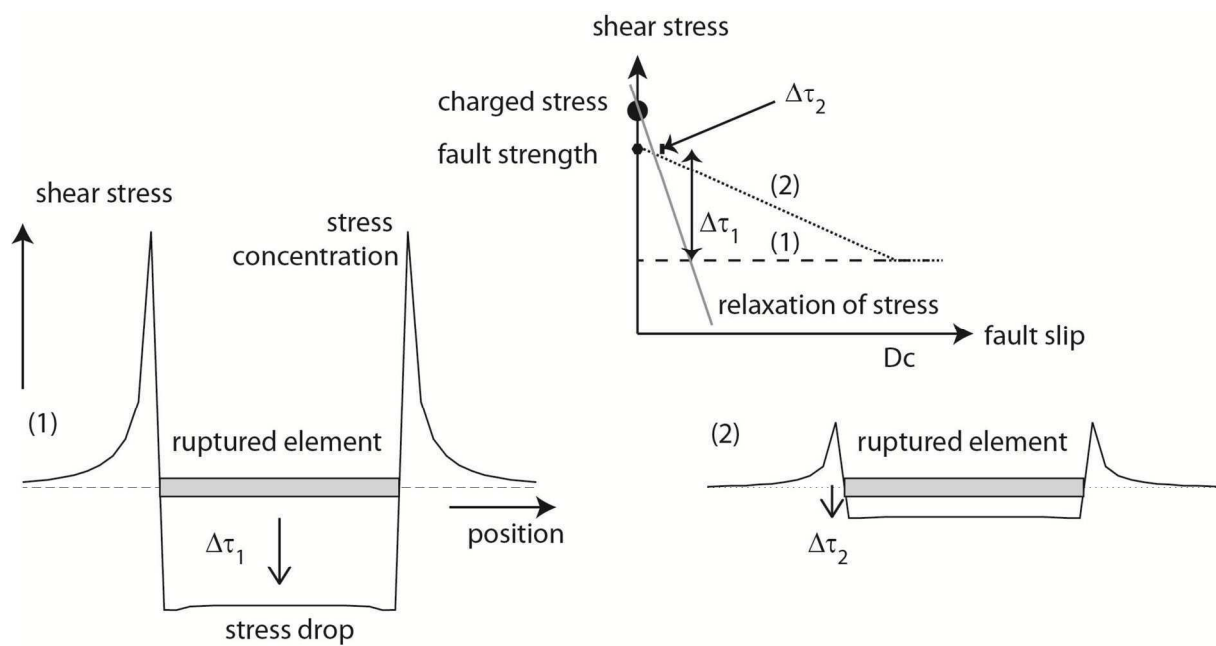
1 Figure A3



2

3

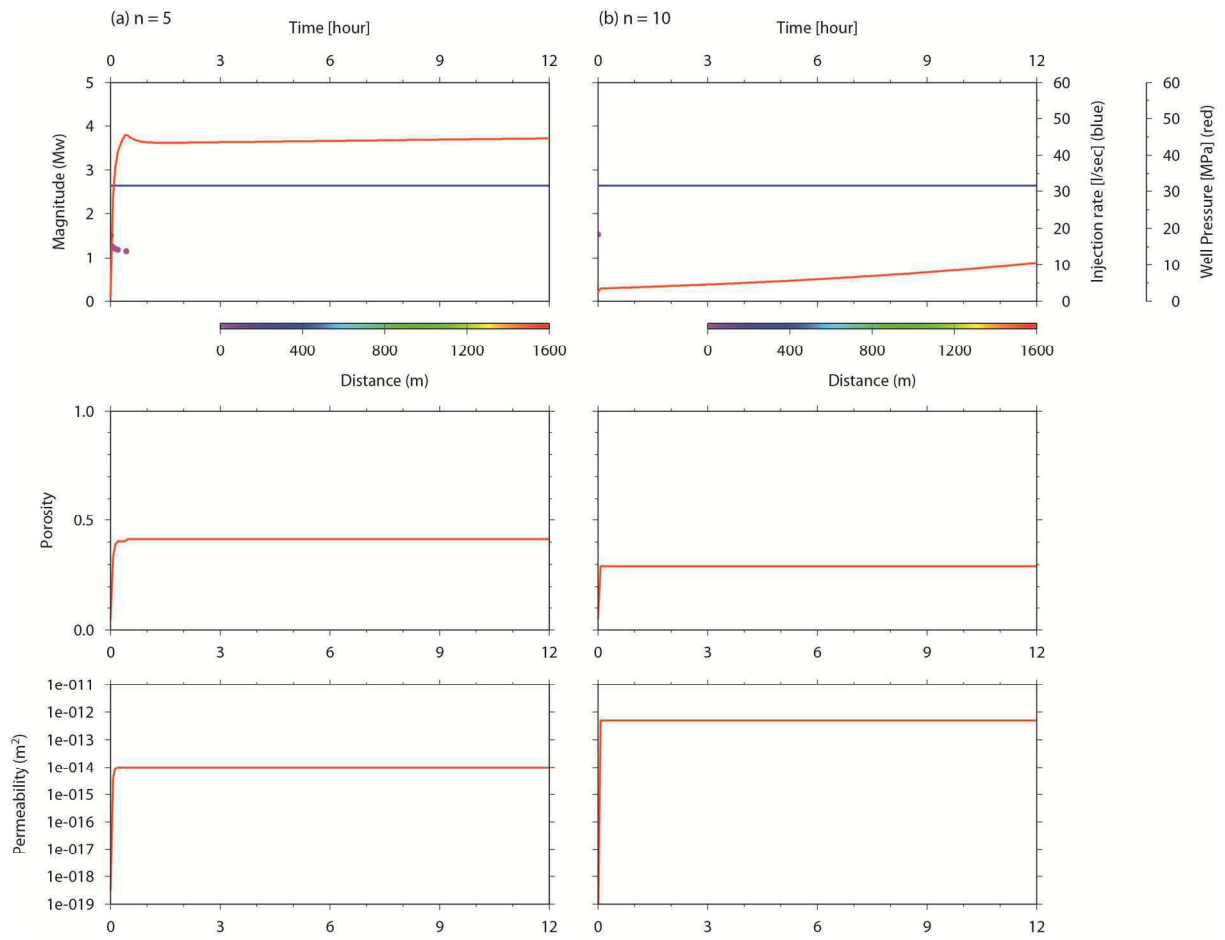
1 Figure A4 :



2

3

1 Figure A5 :



2